

REPORT DOCUMENTATION PAGE			<i>Form Approved</i> OMB No. 0704-0188		
Public reporting burden for this collection of information is estimated to average 1 hour per response, including the time for reviewing instructions, searching existing data sources, gathering and maintaining the data needed, and completing and reviewing this collection of information. Send comments regarding this burden estimate or any other aspect of this collection of information, including suggestions for reducing this burden to Department of Defense, Washington Headquarters Services, Directorate for Information Operations and Reports (0704-0188), 1215 Jefferson Davis Highway, Suite 1204, Arlington, VA 22202-4302. Respondents should be aware that notwithstanding any other provision of law, no person shall be subject to any penalty for failing to comply with a collection of information if it does not display a currently valid OMB control number. PLEASE DO NOT RETURN YOUR FORM TO THE ABOVE ADDRESS.					
1. REPORT DATE (DD-MM-YYYY) 15/10/2011		2. REPORT TYPE Final Performance Report		3. DATES COVERED (From - To) 15/10/2005 to 14/01/2011	
4. TITLE AND SUBTITLE PECASE: All-Optical Photonic Integrated Circuits in Silicon			5a. CONTRACT NUMBER		
			5b. GRANT NUMBER FA9550-06-1-0003		
			5c. PROGRAM ELEMENT NUMBER		
6. AUTHOR(S) Professor Ali Adibi e-mail:adibi@ee.gatech.edu Tel: (404) 385-2738 Fax: (404) 894-4641			5d. PROJECT NUMBER		
			5e. TASK NUMBER		
			5f. WORK UNIT NUMBER		
7. PERFORMING ORGANIZATION NAME(S) AND ADDRESS(ES) Georgia Institute of Technology School of Electrical and Computer Engineering Atlanta, GA 30332-0250			8. PERFORMING ORGANIZATION REPORT NUMBER		
9. SPONSORING / MONITORING AGENCY NAME(S) AND ADDRESS(ES) AFOSR / RSE 875 North Randolph Street, Suit 325 Room 3112 Arlington, Virginia 22203-1768			10. SPONSOR/MONITOR'S ACRONYM(S) AFOSR / RSE		
			11. SPONSOR/MONITOR'S REPORT NUMBER(S) AFRL-OSR-VA-TR-2012-0016		
12. DISTRIBUTION / AVAILABILITY STATEMENT Distribution A					
13. SUPPLEMENTARY NOTES					
14. ABSTRACT <p>This progress report summarizes achievements in Dr. Adibi's research group at Georgia Institute of Technology in the area of All-Optical Photonic Integrated Circuits in Silicon, supported by Air Force Office of Scientific research (AFOSR) PECASE award since December 2005. Only major achievements with very brief description are listed in this report. Detailed information can be found in the recent publications or can be directly requested from Dr. Adibi.</p> <p>This AFOSR-supported research was started in December 2005 and is directed toward exploiting and enhancing the linear and nonlinear optical properties of silicon micro/nano cavities for chip-scale sensing and signal processing. To achieve this goal, in what follows, different steps (including theoretical and modeling tools development, microcavity fabrication and characterization techniques, and methods to develop chip-scale devices) to realize this chip-scale signal processing will be discussed. Our research in this field has already resulted in a number of scientific publications and technical presentations. A complete list of journal papers and conference presentations is included at the end of this report. AFOSR support has been acknowledged in all these publications and presentations.</p>					
15. SUBJECT TERMS Standard terms apply					
16. SECURITY CLASSIFICATION OF:			17. LIMITATION OF ABSTRACT UU	18. NUMBER OF PAGES	19a. NAME OF RESPONSIBLE PERSON Gernot S. Pomrenke RSE (Program Manager)
a. REPORT U	b. ABSTRACT U	c. THIS PAGE U			19b. TELEPHONE NUMBER (include area code) 703.696.8426

**Final Report to the
Air Force Office of Scientific Research (AFOSR)**

PECASE: All-Optical Photonic Integrated Circuits in Silicon

Georgia Institute of Technology

Principal Investigator:

Ali Adibi

*Professor, School of Electrical and Computer Engineering,
Georgia Institute of Technology
Atlanta, GA 30332-0250
e-mail: adibi@ee.gatech.edu
Tel: (404) 385-2738
Fax: (404) 894-4641*

I. Introduction

This progress report summarizes achievements in Dr. Adibi's research group at Georgia Institute of Technology in the area of All-Optical Photonic Integrated Circuits in Silicon, supported by Air Force Office of Scientific research (AFOSR) PECASE award since December 2005. Only major achievements with very brief description are listed in this report. Detailed information can be found in the recent publications or can be directly requested from Dr. Adibi.

This AFOSR-supported research was started in December 2005 and is directed toward exploiting and enhancing the linear and nonlinear optical properties of silicon micro/nano cavities for chip-scale sensing and signal processing. To achieve this goal, in what follows, different steps (including theoretical and modeling tools development, microcavity fabrication and characterization techniques, and methods to develop chip-scale devices) to realize this chip-scale signal processing will be discussed. Our research in this field has already resulted in a number of scientific publications and technical presentations. A complete list of journal papers and conference presentations is included at the end of this report. AFOSR support has been acknowledged in all these publications and presentations.

II. Research Accomplishments

II.A. Systematic design and fabrication of high-Q Microresonators in Si and SiN

II.A.1 Theoretical study and demonstration of high-Q resonators in Si

Recently, ultra high Q silicon undercut microdisk resonators were demonstrated, and a detailed study of the many of the non-idealities of the high Q silicon microdisk structures including intrinsic material absorption, Rayleigh scattering from surface roughness due to fabrication imperfections, and surface state absorption was presented. However, the implementation of microdisk structure in was limited to undercut microdisk resonator geometry. In such an undercut microdisk, the SiO_2 layer beneath the Si microdisk is etched resulting in the removal of the silica substrate, and therefore, the microdisk is left isolated from the surrounding. Such undercut microdisk architecture exhibits several challenges in terms of integrating with active electronic functionalities such as metal-oxide-semiconductor (MOS) transistors and p-n junction. Furthermore, the narrow SiO_2 post supporting the undercut microdisk, results in a large thermal resistance from the active microdisk cavity to the Si substrate. Hence, this results in thermal bistability and other unwanted non-ideality as we increase the input optical power impinging on the microdisk cavity. Another challenge with the undercut structures is the difficulty in having a robust and suspended silicon waveguide coupled to the disk.

For the goal of integrating several chip-scale functionalities with the microdisk resonator it is essential to use Si-based waveguides for input/output coupling to the microdisk resonator. While undercutting a microdisk resonator is relatively easy, using an undercut waveguide for coupling light to such an undercut resonator is not trivial. For mechanical stability and low-loss performance of the integrated photonic structures it is highly desirable to keep the SiO_2 layer underneath the Si structures intact. In a recent work, by developing advanced fabrication techniques, we were able to implement and experimentally demonstrate a Si microdisk resonator on a substrate with a $Q \sim 0.5 \times 10^6$. This motivated us to investigate the impact of silica substrate on the Q of the resonator.

In order to assess the impact of the silica substrate, we performed a detailed theoretical study on the effect of oxide substrate on the Q of the microdisk resonator. Two structures were considered for this study, namely a conventional SOI microdisk as shown in Figure 1.a, where the Si layer is completely etched, and a microdisk on Si pedestal as shown in Figure 1.b, where the Si layer is partially etched and as a result a thin Si pedestal layer is left underneath the microdisk. In the rest of the paper we refer to these two architectures as conventional and pedestal microdisks respectively.

There are two main advantages of the pedestal microdisk, namely the silicon pedestal reduces the thermal resistance of the microdisk and also facilitates its integration with active electronics such as MOS transistors and p-n junctions. For instance, nonlinear optical applications in silicon suffer from optical power limitations due to two-photon absorption (TPA) generated free carriers. Using the pedestal microdisk architecture, we could potentially integrate a reverse-bias p-n junction with the resonator and sweep the TPA-generated free-carriers away from the microdisk active region.

In the simulations of the structures in Figures 1.a and 1.b, we used the finite-element method (FEM) with incorporation of a perfectly matched layer (PML) absorbing boundary condition. The simulation for a microdisk with a Si of thickness 230 nm and a radius 10 μm resulted in a radiation $Q > 10^{10}$. For the pedestal microdisk, similar results were obtained. Therefore, we conclude that the ultimate limit on the achievable Q is limited mostly by the fabrication limitation and other non-idealities in the device and not by the radiation into the SiO_2 layer. The major non-idealities are: 1) two-photon absorption assisted free-carrier generation, 2) surface absorption due to the simultaneous presence of sidewall roughness and surface electronic states, and 3) thermal resistance. Thus, our theoretical results suggest that this high Q 's obtained for undercut microdisk structures, should be achievable in the microdisk-on-oxide structures (without undercutting). To investigate this observation experimentally, we performed more improvement on the fabrication steps and implemented a series of microdisk resonators with 20 μm radius on a SOI wafer.

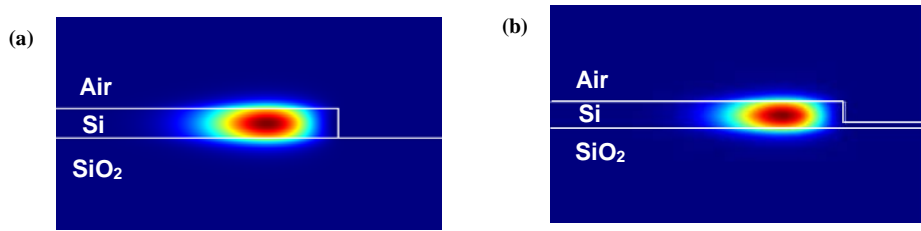


Fig. 1. (a) The cross section of a Si microdisk resonator on oxide substrate, the silicon thickness is 230 nm. (b) The cross section of a pedestal microdisk resonator on oxide substrate; the Si shallow and deep layers have the thicknesses of 60 nm and 225 nm respectively. The energy profile of the fundamental radial TE (electric field predominantly in the plane of the microdisk) mode is shown in the figures. In both cases the disk radius is 20 μm .

Device fabrication

By developing a fine etching and fabrication recipe, we were able to fabricate microdisk cavities with smooth sidewalls on SOI. Figure 2 shows the structure of the microdisk resonator coupled to a ridge waveguide. The structure is fabricated on SOITEC SOI with device thickness of 250 nm and buried oxide (BOX) thickness of 3 μm . Fabrication steps starts with growing a 60 nm

thermal oxide on SOI wafer as a hardmask. An electron-beam resist ZEP-520A with a thickness of 350 nm is spin coated on the wafer. Then, the structure pattern is transferred onto the wafer using a JEOL-9300 electron-beam-lithography system. Prior works in high Q Si microdisks have used the resist reflow process to smooth the microdisk sidewall. In this work, we do not use this process due to the tight resolution requirements for the waveguide-resonator gap, and controlling the sidewall angle in the waveguide and the resonator.

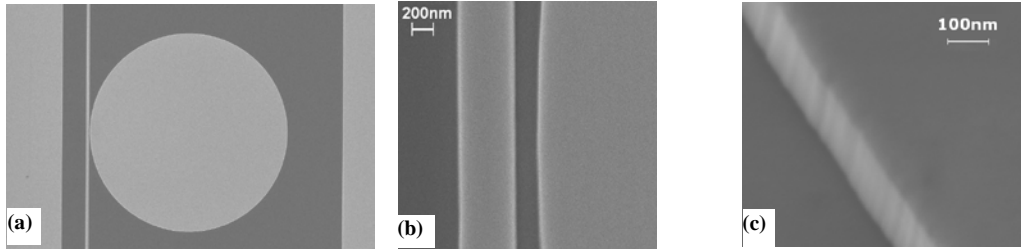


Fig. 2. (a) SEM micrograph of a Si microdisk resonator side-coupled to a waveguide; the disk radius is 20 μm and its thickness is 225 nm. The waveguide width is 550 nm and the gap between the disk and the waveguide is 220 nm. (b) A closer view of the structure at the waveguide-cavity coupling region. (c) Sidewall of the microdisk captured at an azimuth angle 30° and sample tilt angle 30°.

In order to define the structure, a two-step etching process is used. The first step is to etch the hard mask with $\text{CF}_4/\text{CHF}_3/\text{Ar}$ gases in inductively coupled plasma (ICP). Then, the resist left on top of the structure is removed and therefore an oxide layer is left on top of the structure as a hardmask. The final step is etching the silicon with Cl_2 in the ICP chamber. The resulting structure as shown in Figure 2 is a microdisk with radius of 20 μm , a ridge waveguide with width 550 nm and the gap between the microdisk and the waveguide is 220 nm. The measured sidewall angle was more than 85°. The thickness of the silicon is 225 nm and a thin layer of thermal oxide is left on top of the structure. The effect of this thin thermal oxide on the top of the microdisk may improve the interface properties and consequently the Q of the cavity. This issue is under more investigation.

Experimental results

Figure 3(a) shows the spectrum of the microdisk resonator shown in Figure 2. The measurement was done using a swept-wavelength test setup. A fiber polarization controller followed by a polarizer was used to control the input polarization state to the device. We used standard objective lens for coupling into and out of the device. Conventional adiabatic tapering was used at the waveguide input facet in order to reduce the insertion loss. Unless otherwise specified, all the measurement results reported in this paper use the TE-polarized light. The laser scan rate was slower than the cavity loading time in order to allow efficient cavity build-up and to obtain meaningful resonance spectrum. During each measurement cycle, the laser was repeatedly scanned several times over the resonant feature to monitor the variations in the resonance spectrum. As can be seen from Figure 3(a), several different resonant modes with Q 's ranging from 1.5×10^5 up to 2.0×10^6 were observed, corresponding to different radial mode orders. Based on the resonance wavelength observed in experiment and theory, we could identify the radial mode order of each of the high Q modes in Figure 3(a).

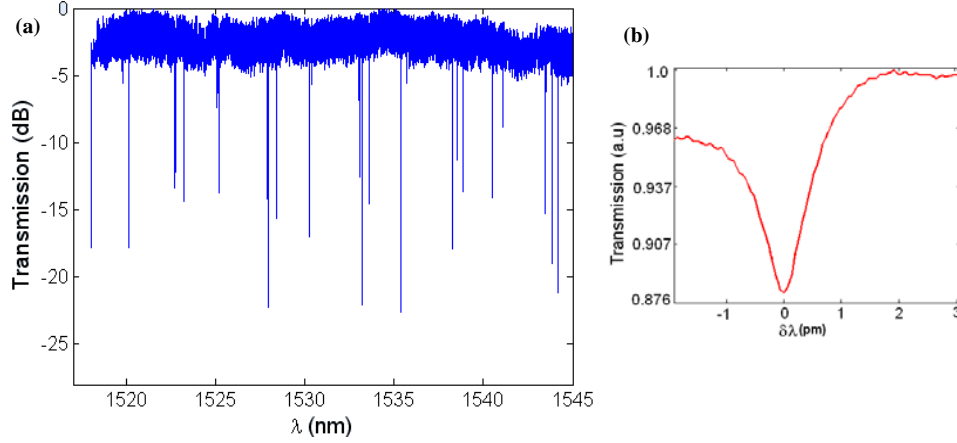


Fig. 3. (a) Spectrum of the microdisk resonator shown in Figure 2 for TE polarization. (b) An ultra-high $Q=2 \times 10^6$ was observed for the 2nd order radial mode at resonance $\lambda=1520.188$ nm. The location of the resonance in the experiment corresponds with the simulation results.

The first few radial mode orders, observed in the experiment, all exhibited a $Q \geq 10^6$. Figure 3.b shows the maximum $Q \sim 2 \times 10^6$ that was observed. To our knowledge, this is the highest Q reported for a planar silicon microdisk of this radius for conventional disk-on-substrate. The power extinction for each of these resonant modes varies, due to deviations from the critical coupling condition caused by changes in the waveguide-cavity coupling as well as changes in the intrinsic Q of these modes.

Pedestal microdisks, such as the one shown in Figure 1(b), were also fabricated and characterized. The disk radius and the input/output coupling waveguide are identical to the microdisk shown in Figure 2, with the only difference being that by controlling the etching depth of the microdisk, we leave a thin pedestal layer of silicon under the resonator. FEM simulations show that the radiation Q of this structure is very large ($Q > 10^{10}$). Hence, we anticipate that the Q is limited only by the fabrication imperfections, surface roughness, and other non-idealities. Figure 4 shows the SEM cross section of this device. From the SEM measurement, the thickness of the thin pedestal layer, after the fabrication, was in the range $63 \text{ nm} \pm 3 \text{ nm}$. As can be seen from this figure, trenching is observed at the interface of the device and the pedestal layer. This trench formation, which is typical in Cl_2 chemistry based plasma etching of silicon, can be further reduced by more optimization of the Si etch recipe.

Figure 5.a shows the spectrum of this pedestal microdisk. Figure 5.b shows the resonance spectrum of the 2nd order radial mode. As it can be seen from this figure, resonance splitting is observed for this mode. Lorentzian fitting, taking resonance splitting into account, yielded an intrinsic (unloaded) Q of about 3.0×10^6 in this pedestal microdisk architecture. This, to our knowledge, is the first demonstration of this unique microdisk architecture, and is also the highest recorded Q for a microdisk cavity on substrate. We anticipate this pedestal microdisk to be an enabling device platform suitable for integration with p-n junctions and other active electronic components with great potential to be used for modulation and switching applications.

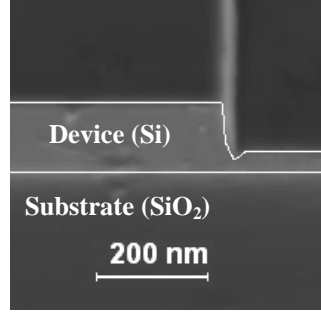


Fig. 4. SEM cross section of the pedestal type structure captured at a sample tilt angle of 30° . The microdisk radius and thickness are $20\ \mu\text{m}$ and $225\ \text{nm}$ respectively, and the thickness of the shallow pedestal layer is $65\ \text{nm}$.

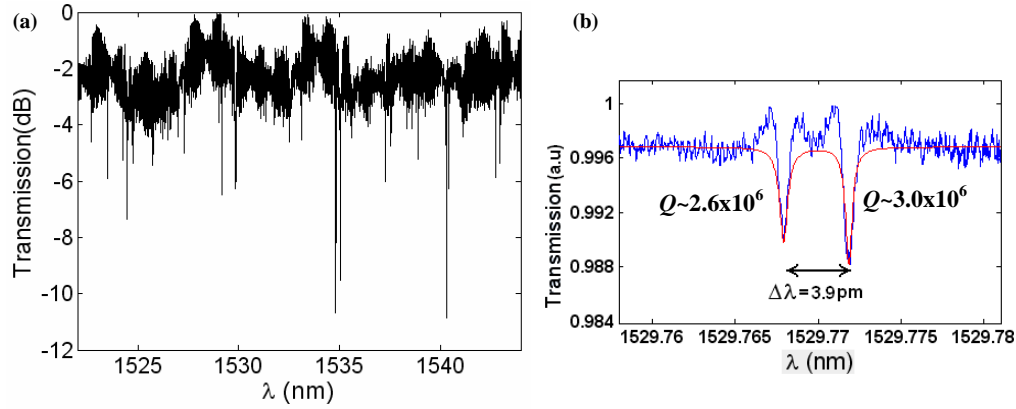


Fig. 5. (a) Spectrum of the pedestal microdisk resonator coupled to a waveguide for TE polarization. (b) Spectrum of the 2nd order radial mode; mode-splitting due to the coupling of CW and CCW is observed. The disk radius and the input/output coupling waveguide are identical to the conventional microdisk shown in Figure 2.

Ultra high Q resonator on a thin SiO₂ substrate

In our previous experiments the thickness of the oxide substrate was $3\ \mu\text{m}$ to guarantee the optical isolation of the microdisk from the underneath Si bulk layer. As will be discussed later, a major challenge in ultra high Q resonator is thermal stability of the resonator which requires a large conductivity to suppress the thermal instability and spectral broadening. The presence of the substrate improves the thermal conductivity by transferring the heat from the microdisk to the underneath bulk Si layer. Although a thinner oxide substrate results in a better conductivity, it can increase the radiation of the cavity electromagnetic mode to the underneath Si layer.

Our FEM simulations for a microdisk on a $1\ \mu\text{m}$ oxide thickness show an intrinsic $Q \sim 10^9$. Therefore, the cavity Q is not limited by a substrate with this level of thickness, and still the fabrication imperfection and other non-idealities limit the Q. To experimentally investigate this fact, we fabricated a new series of microdisk resonators on a SOI wafer with a $1\ \mu\text{m}$ thickness. Figure 6 shows the SEM image of such a microdisk. It is a pedestal type as schematically explained in Fig. 1(b). The fabrication process steps were as explained in Section 3 with adding one more step at the end to improve the sidewall roughness and surface properties. In this step the sample, after 5 min Piranha cleaning, was put in the dry oxidation furnace at a temperature of 850°C . A thin layer of oxide was grown on the disk surfaces to improve the smoothness of the sidewalls. This process also recovers the crystal planes of Si at the microdisk sidewalls, which

were damaged during the plasma etching. As a result, the electronic surface states at the disk sidewalls are dramatically reduced and therefore surface absorption is reduced. Consequently, the Q of the cavity is improved.

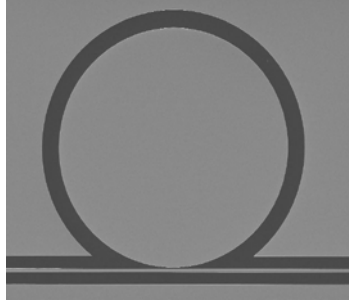


Fig. 6. Structure of a pedestal microdisk resonator coupled to a waveguide. The disk has a radius of $20\ \mu\text{m}$ and a thickness $210\ \text{nm}$ and it is seated on a Si pedestal with a thickness of $40\ \text{nm}$. The waveguide width is $500\ \text{nm}$, and the gap between the waveguide and the disk is $120\ \text{nm}$.

Figure 7 shows the spectrum of the pedestal microdisk shown in Fig. 6. As it can be seen from Fig. 7(a), several high Q features are observed in the spectrum in the critical coupling regime. Figure 7(b) shows the one of the resonance modes of the disk with an unloaded $Q=3.1 \times 10^6$ in the critical coupling regime. No mode splitting is observed for this ultra-high Q resonance. This is the highest Q reported for a Si disk on a substrate for including both conventional and pedestal architectures. In addition, this is the highest Q reported for a disk in the critical coupling regime with a planar integrated waveguide-cavity coupling.

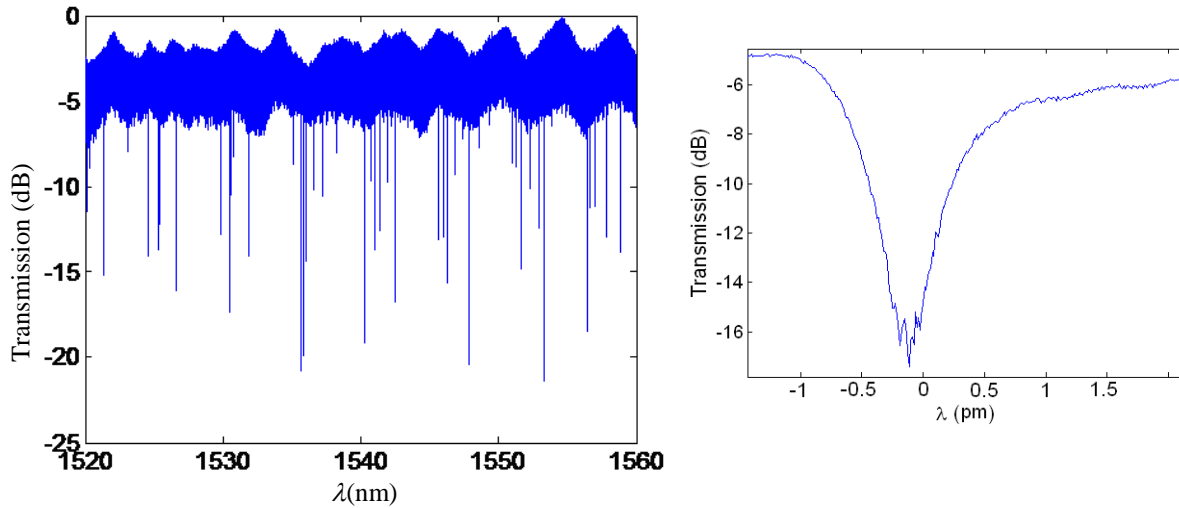


Fig. 7. (a) Spectrum of a pedestal microdisk resonator shown in Fig. 7. (b) Spectrum of a resonance mode with an unloaded $Q=3.1 \times 10^6$ in the critical coupling regime.

The next steps is to going to thinner substrate as well as adding more post-processing steps to the fabrication to reduce microdisk sidewalls roughness and the electronic surface states.

Systematic design of waveguide-resonator coupling

In a TWR-waveguide structure, in the weak coupling regime, the power transmission and the total loaded quality factor (Q_L) at resonance are respectively expressed as:

$$T(\omega_0) = \frac{P_{out}}{P_{in}} = \left| \frac{1 - Q_0/Q_c}{1 + Q_0/Q_c} \right|^2$$

In the above expression Q_0 and Q_c are respectively the intrinsic quality factor and coupling quality factor, with the coupling quality factor (Q_c) being used as a measure of rate of energy decay from the cavity to the waveguide, i.e. stronger coupling between the waveguide and the cavity results in smaller Q_c . As it can be seen from Eq. (1), in order to completely transfer energy from waveguide to the resonator at the resonance, Q_0 and Q_c should be equal. This condition is also referred to as critical coupling.

In a TWR-waveguide coupling structure, Q_c depends on coupling interaction length, field extension of the field outside the resonator and the waveguide, and effective mode index matching between the waveguide and TWR modes. Since the microdisk resonator is a TWR structure, we can ascribe to each microdisk mode, a phase and an associated effective mode index. In the case of the large index mismatch between the microdisk and the waveguide, coupling can be strongly reduced, so much so that even bringing the waveguide very close to the cavity does not significantly alter their coupling. Moreover, putting the waveguide and resonator too close to each other results in strong perturbation of the cavity structure, resulting in additional loss and the thus, degradation of the Q . In order to illustrate this coupling and index matching issue, using the coupled mode analysis, we consider the microdisk and waveguide whose dimensions are given in the captions of Fig. 2.

Figure 8(a) shows the effective mode index for different radial modes of this microdisk. The effective index of the fundamental TE mode of the waveguide is also shown in this figure. As it can be seen, the 3rd order radial microdisk mode has an effective index that is closer to that of the waveguide. Hence, we expect this mode to be better phase matched to the waveguide mode, thereby resulting in a strong coupling. Figure 8(b) shows the calculated coupling Q (Q_c) for different waveguide-cavity gaps, based on a coupled-mode formalism and using the FEM calculated field profiles for the disk and waveguide. As it can be seen from Fig. 8(b), the 3rd order radial mode has a lower value of Q_c , thereby confirming the prediction of better waveguide-cavity coupling, i.e. closer to critical coupling, than the lower order modes based on the phase-mismatch obtained from effective indices in Fig. 8(a). For a gap of 220 nm, for the 1st order radial mode, Q_c was calculated to be 40×10^6 . Therefore, it is reasonable not to be critically coupled to the fundamental mode for these waveguide-resonator geometry parameters. The same argument applies for the 2nd and 3rd order modes. However, for the gap of 150 nm, the values of Q_c vary in the range of 1×10^6 - 10×10^6 and are closer to what we may achieve for the intrinsic Q of the cavity, thereby ensuring we are closer to critical coupling.

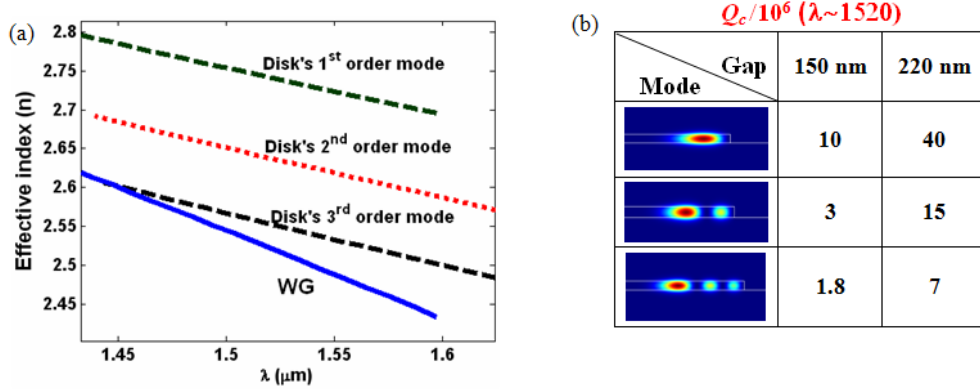


Fig. 8. (a) Comparison of the effective indices of the traveling TE modes of the microdisk resonator shown in Fig. 2 for different radial mode orders with that for the waveguide. The dimension of the disk radius and the waveguide is given in the caption of Fig. 2. (b) Q_c for different gaps between the waveguide and the microdisk calculated using coupled mode theory.

Although, the optimization of phase matching can improve the coupling strength, but as shown in Fig. 8, the values of coupling Q are still large, especially, for the fundamental mode which is the mode of interest in many applications. Therefore, more engineering needs to be performed on the geometry of the structure to adjust the coupling Q to the desired level. One possible way is to add the pedestal layer to the structure which brings another degree of freedom into the design. We have already shown ultra-high Q in the pedestal microdisk architecture. Here, we show that a non-zero pedestal thickness can dramatically reduce the coupling Q . Figure 9 shows the schematic cross section of a pedestal microdisk coupled to a waveguide. Figure 10 shows the variation of coupling Q for such pedestal microdisk coupled to the waveguide for different mode orders. The disk radius is 20 μm and the pedestal thickness is 40 nm. The total thickness of the Si layer is 230 nm. The calculations were performed for a waveguide with the widths of 540nm and 500nm respectively. As shown in Fig. 10, the presence of the pedestal layer has dramatically reduced the coupling Q into a tangible range comparable with the intrinsic Q achieved in the fabrication.

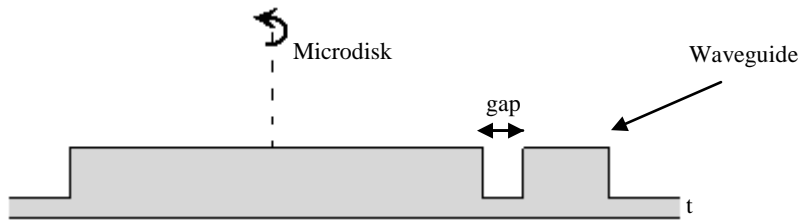


Fig. 9. Cross section of a pedestal microdisk resonator coupled to a waveguide.

Hence, adjusting the thickness of the pedestal layer adds another degree of freedom to dramatically modify the coupling Q while the ultra-high Q property of the resonator is preserved. This pedestal architecture can also be applied to a microring resonator structure which is discussed in the next section.

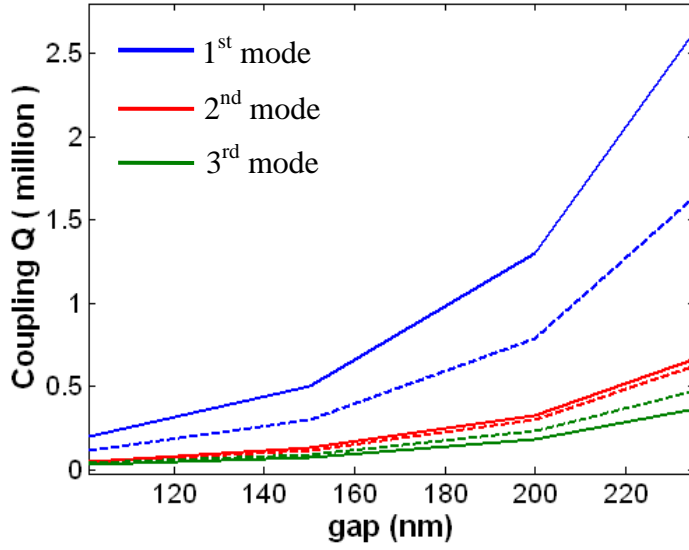


Fig. 10. Variation of the coupling Q for different disk mode orders, as shown by different colors, for a pedestal microdisk coupled to a waveguide, as shown in Fig. 13. The disk has a radius of $20\ \mu\text{m}$ and the pedestal thickness is $t=40\text{nm}$. The solid and dash curves correspond to waveguide widths of 540nm and 500nm respectively.

Figure 11(a) shows the SEM image of a microring resonator with a radius $5\ \mu\text{m}$ and the width 500nm coupled to a waveguide with the same width. The thickness of both the waveguide and the disk is $250\ \text{nm}$. Figure 11 (b) shows the schematic cross section of such structure in which a pedestal layer is beneath the ring and the waveguide. In the case that the thickness of the pedestal layer is zero, the coupling Q for such structure at a resonance around $1550\ \text{nm}$ is 1.3 million as shown in Fig. 11(c). In practice, for such fabricated microring structure the intrinsic Q is less than 10^5 . Therefore, such a large difference, between the coupling Q and the intrinsic Q , results in weak power exchange between the waveguide and the ring. As shown in Fig. 11(c), adding the pedestal layer dramatically reduces the coupling Q into a practical range. Figure 11(d) shows the calculation of coupling Q for a pedestal thickness of 40nm and two different waveguide widths of $500\ \text{nm}$ and $440\ \text{nm}$. As it can be seen from Fig. 15(d), coupling Q for the waveguide with the $440\ \text{nm}$ width is less than that of $550\ \text{nm}$ width waveguide. This is because of larger field extension of 440nm width waveguide in the transverse direction and therefore larger interaction with the microring. Hence, by adjusting the thickness of the pedestal layer and the width of the waveguide the desired coupling Q in the practical range can be obtained.

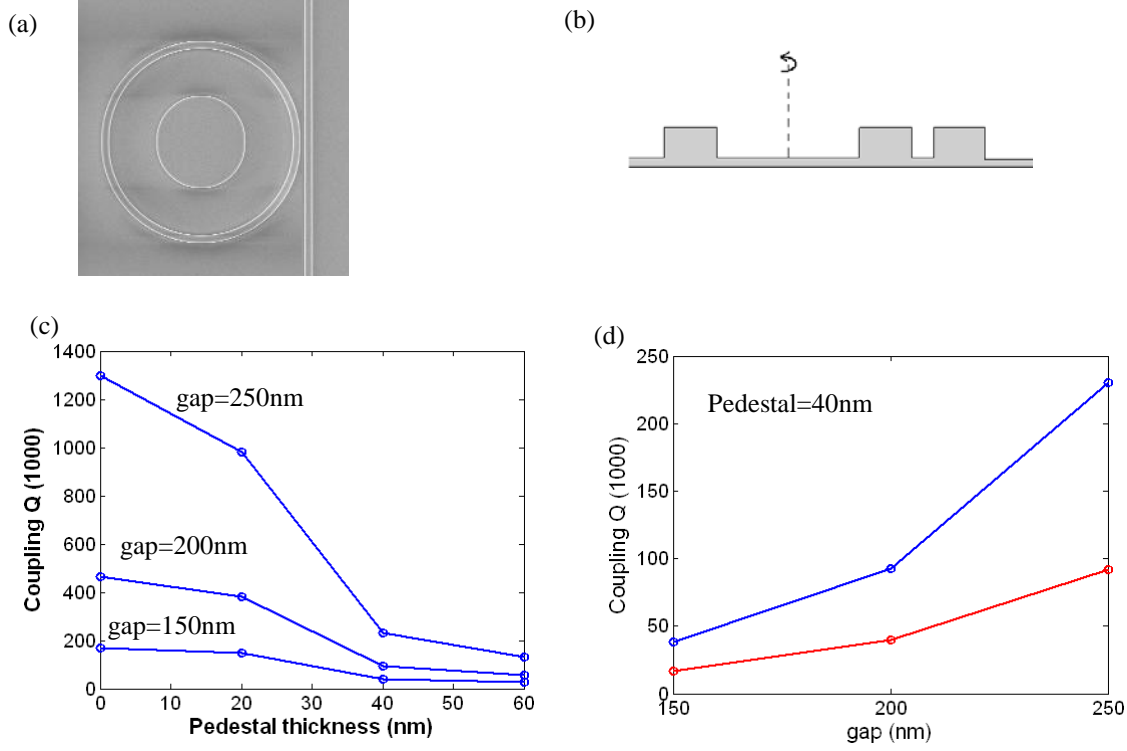


Fig. 11. (a) SEM image of a microring resonator, with a $5\ \mu\text{m}$ radius, coupled to a waveguide with a $500\ \text{nm}$ width. The gap between the waveguide and the ring is $250\ \text{nm}$. (b) Schematic cross section of this coupling structure. A pedestal layer with an arbitrary thickness is beneath the microring and the waveguide. (c) Calculation of coupling Q for different pedestal thicknesses and different gaps. (d) Variation of coupling Q versus gap for a pedestal thickness of $40\ \text{nm}$; the blue and the red curve correspond to waveguide widths of $500\ \text{nm}$ and $440\ \text{nm}$ respectively.

II.A.2 Systematic design and fabrication of high- Q single-mode pulley-coupled planar silicon nitride microdisk resonators at visible wavelengths

Integrated nanophotonics in the visible range of the spectrum is critical for several applications in sensing and optical signal processing (e.g. biosensing using fluorescence and surface enhanced Raman spectroscopy (SERS) and signal processing for LiDAR). Unlike silicon, low Si content, LPCVD Si_3N_4 offers a very low-loss material throughout the optical range (wavelengths from $300\ \text{nm}$ to several microns), and a moderately high refractive index ($n \approx 2$). Si_3N_4 , being a dielectric material, does not suffer from free carrier absorption, which is an important limiting factor in Si high- Q resonators. During this period of the PECASE award, we focused on monolithic, high Q , compact $\text{Si}_3\text{N}_4/\text{SiO}_2$ resonators in the visible range, and critical coupling of the resonators to in-plane waveguides was also demonstrated (at $\lambda = 652\text{--}660\ \text{nm}$). We also report optimized coupling structures using pulley-shaped concentric waveguides to enable radial mode-selective coupling and the potential for over-coupled resonator structures.

Fabrication of these microdisk structures uses a Si substrate with a thermally grown $6\ \mu\text{m}$ oxide layer, which isolates the guiding Si_3N_4 layer from the lossy Si substrate. A $200\ \text{nm}$ -thick layer of low-loss, stoichiometric Si_3N_4 is deposited using low pressure chemical vapor deposition (LPCVD). We use $500\ \text{nm}$ of ZEP-520 electron beam resist with a thin layer of espacer $300\ \text{nm}$ to

inhibit surface charge-up. The waveguides and microdisks are patterned using the electron beam lithography system with the pattern addressing grid size of 1 nm and the beam current set to $I=2$ nA (using 60 μm aperture). Choosing a dosage of $D=250$ $\mu\text{C}/\text{cm}^2$ for the ZEP, the smallest possible shot pitch (SP) is 4 nm ($\text{SP} \geq [I/(f \cdot D)]^{1/2}$). Moreover, the beam spot size for the 2 nA current is approximately 6 nm. We expect that with such a shot pitch and beam spot size, the roughness introduced to the microdisk and waveguide structures during the electron beam lithography is smaller than 10 nm. This is important in order to obtain low-loss high-fidelity devices. The patterned structures are etched using CF_4 gas in an STS inductively coupled plasma (ICP) etcher with the optimized process parameters which minimize the sidewall roughness (Pressure=5 mTorr, Coil Power =600 W, and Platen Power=20 W). The sidewall roughness is inspected with scanning electron microscopy (SEM), and the sidewall tilt angle is measured to be greater than 85 degrees (as shown in Fig. 12).

The microdisk resonators are characterized by a tunable laser swept across the 652–660nm wavelength range. We note here that the flexibility in the optical properties of the Si_3N_4 layer allows us to target the designs for any other wavelength ranges within the transparency window of the Si_3N_4 layer, for future applications and the wavelength range reported here is chosen primarily due to our existing tunable laser in our laboratory.

When the waveguide is side-coupled to the resonator at a single point, the critical coupling condition requires a very narrow coupling gap (gap< 100 nm) between the waveguide and the resonator. In order to ease the fabrication, we have proposed a rib-like configuration in which a thin layer of the guiding material (Si_3N_4) (that is achieved by partial plasma dry etching) increases the field overlap between the coupled elements thus increasing the coupling coefficient [1]. Nevertheless, such rib-type structures require an accurate control over the etch depth to achieve the targeted “pedestal” height. In addition, single-mode operation is hard to achieve in such rib-type structures. Another effective, yet seldom investigated approach to increase the gap size and thus ease the fabrication is increasing the effective coupling length rather than the field overlap. In this approach, termed “pulley” coupling, the waveguide wraps around the resonator (e.g., a microdisk), effectively increasing the coupling length several times compared to the single point coupling with a straight waveguide. This approach was initially modeled with conformal transformation method [2] and recently utilized in a chalcogenide glass sensor [3].

However, a thorough investigation of this technique is needed to develop a systematic design approach for high Q resonators with whispering gallery modes. In this work, a systematic analysis of pulley-coupled, high Q, $\text{Si}_3\text{N}_4/\text{SiO}_2$ resonators is presented. We also demonstrate the coupling of the resonators to wrap-around waveguides in the visible wavelength range (at 652–660 nm). We will show that not only are wider coupling gaps possible using the pulley coupling scheme, but also the strict phase matching condition makes the coupling single mode. Therefore, with the proper choice of the wraparound waveguide width, only one of the radial modes of the microdisk is excited while the other radial modes are uncoupled from the waveguide field. These advantages (single mode operation, critical coupling with easy-to-fabricate gap size, and high Q) make the resonance structures presented here an excellent choice for applications that require strong light matter interaction. The transmission spectra of the devices in Fig. 12 are shown in Fig. 13.

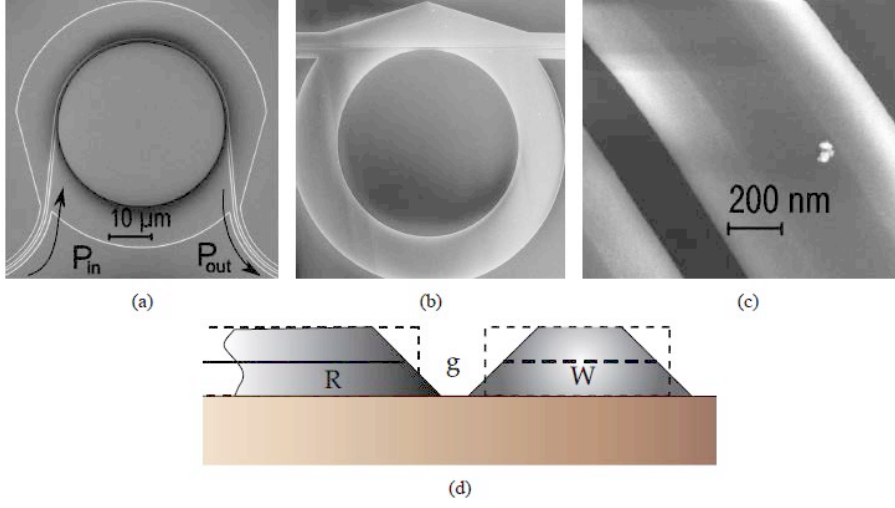


Fig. 12. (a) The pulley coupling configuration in which the waveguide wraps around the microdisk resonator to increase the effective coupling length. The phase matching to different radial modes of the microdisk is achieved by the choice of the waveguide width. (b) The conventional straight coupling configuration in which the waveguide couples to the microdisk only at a single point. In this configuration the effective interaction length is significantly shorter than the pulley scheme depicted in (a), making the coupling much less sensitive to the phase matching condition. (c) Top view of an SEM image of a waveguide etched on a 200 nm layer of Si_3N_4 on top of an isolating SiO_2 layer on a Si substrate with a 5 minute reflow of the resist. The reflow process leads to smooth but tilted sidewalls. (d) The diagram showing the effect of the reflow process on the waveguide and the microdisk sidewalls.

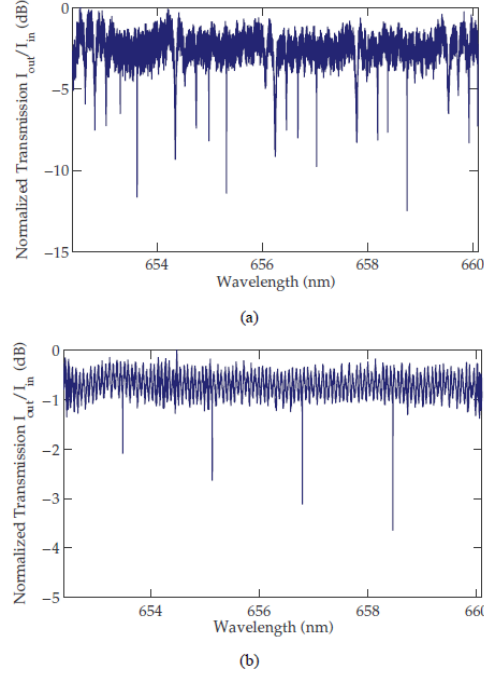


Fig. 13. (a) The normalized transmission spectrum of a 20-micron-radius Si_3N_4 microdisk side coupled to a waveguide with a single point coupling scheme [see Fig. 12(b)]. The coupling gap is 100 nm and several radial TE modes of the microdisk are excited. The waveguide width is 400 nm. The effective coupling length is about $4 \frac{1}{4} \mu\text{m}$. The polarization of the input waveguide is TE. (b) The normalized transmission of the waveguides coupled to the same microdisk as in (a) in the pulley configuration shown in Fig. 12(a). The coupling length is $30 \frac{1}{4} \mu\text{m}$ and the coupling gap is 400 nm. The waveguide width is 390 nm and only the second radial order mode of the disk is excited. The strict phase matching condition does not allow the other radial modes of the microdisk to have significant coupling to the waveguide.

To model this numerically, the coupling coefficient between a waveguide and an adjacent cavity is given by the first order temporal perturbation theory as

$$\kappa = \int_{-\theta_o}^{\theta_o} \left[\frac{i\omega}{4} \int_0^W \int_0^d (\epsilon(r,z) - \epsilon_o) \mathbf{E}_{\text{disk}} \cdot \mathbf{E}_{\text{wg}} r dr dz \right] e^{j\theta} d\theta, \quad (1)$$

$$= S \int_{-\theta_o}^{\theta_o} e^{j\theta(k_o n_{\text{wg}} R_{\text{wg}} - m)} d\theta = 2\theta_o S \text{sinc} \left[(k_o n_{\text{wg}} R_{\text{wg}} - m) \frac{\theta_o}{\pi} \right], \quad (2)$$

in which $k_o = 2\pi/\lambda$ is the wavenumber in the free space, and m is the azimuthal mode order of the resonator. It is clear from Eq. (2) that the phase mismatch $(k_o n_{\text{wg}} R_{\text{wg}} - m)$ between the two structures can reduce the coupling coefficient considerably. If the phase matching condition is met (i.e., $k_o n_{\text{wg}} R_{\text{wg}} = m$), the coupling coefficient is a linear function of the coupling length (which is proportional to λ). Conversely, if the phase mismatch builds up to a multiple of π the coupling vanishes no matter how strong the field overlap is. Since the phase velocities of different WGMs of the resonator vary across different radial modes, one can expect the phase matching condition to be mode-dependent. If the effective index of each radial mode is defined as ($n_{\text{disk}} \equiv m/(k_o R_{\text{disk}})$), it is clear that the phase matching is achieved when $n_{\text{wg}} R_{\text{wg}} = n_{\text{disk}} R_{\text{disk}}$. The effective index of the waveguide is controllable by changing the waveguide width (W) within the range $150 \text{ nm} < W < 550 \text{ nm}$ to ensure single mode guiding. Increasing W results in larger effective indices for all waveguide modes. On the other hand, the effective indices of different radial mode orders of the microdisk resonator depend on the geometrical properties of the microdisk. Noting that the lower order modes of the microdisk have higher effective indices, the required W for phase matching is the largest for the fundamental

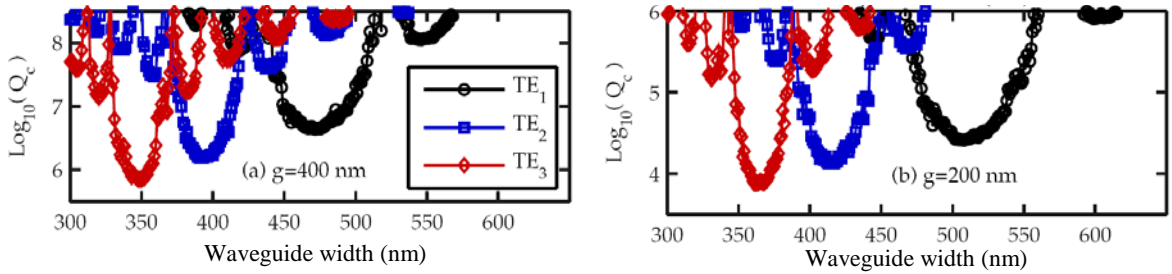


Fig. 14. (a) The simulated coupling quality factor (Q_c) of a $20\mu\text{m}$ radius disk when the waveguide wraps around the disk and the coupling length is $30\mu\text{m}$. As the width of the waveguide is changed, the phase matching condition is met for three different radial modes of the disk. (a) The coupling gap size is 400 nm and the phase matching condition is met for the first three orders of the disk when the waveguide width is 470 , 390 and 340 nm respectively. (b) The gap size is reduced to 200 nm . The coupling is enhanced almost two orders of magnitude for all three modes. As the phase matching condition depends on the radius of the curved waveguide, all microdisk modes are coupled to slightly wider waveguides.

microdisk mode.

To demonstrate the practicality of the optimal design criteria shown in Fig. 14, structures with three different waveguide widths ($W = 470$, 390 , and 340 nm) were fabricated in both single waveguide and add-drop configurations. The waveguides are all single mode for the desired range of wavelengths ($652\text{--}660 \text{ nm}$). Figures 15(a) and 15(b) depict the normalized

transmission for the single waveguides coupled to TE₁ and TE₂ with W of 470 nm and 390 nm, respectively. The coupling gap is 400 nm for all the fabricated structures. To identify the radial mode order in each case in Fig. 15, we compared the measured free spectral range (FSR) with the theoretically calculated FSRs of different radial mode orders. The resonant mode in the structure with $W=470$ nm [Fig. 15(a)] has the largest FSR=1.632 nm, and it corresponds to the TE₁ mode. Similarly the resonant dips in the transmission spectrum of the structure with $W=390$ nm [shown in Fig. 15(b)] correspond to an FSR of 1.658 nm and are attributed to the TE₂ mode.

Finally, Fig. 15(c) depicts the output of the drop waveguide when the through and the drop waveguides are both chosen to be 340 nm wide. In such structures, power is transferred to the drop port only when the third order mode of the microdisk is in resonance. Thus, such an add-drop filter is practically single mode even though the microdisk—unlike a microring—is multimode.

Comparing Fig. 14 and Fig. 15 shows that for each waveguide width design, the waveguide mode couples better to the resonator mode for which stronger coupling (or smaller Q_c) exists. Fig. 14(a) clearly shows that at $W = 470$ nm, 390 nm, and 340 nm, Q_c is the smallest for TE₁, TE₂, and TE₃, respectively. Thus the results shown in Fig. 15 confirm the finding in Fig. 16(a) about the optimal waveguide width (W) for each resonator mode.

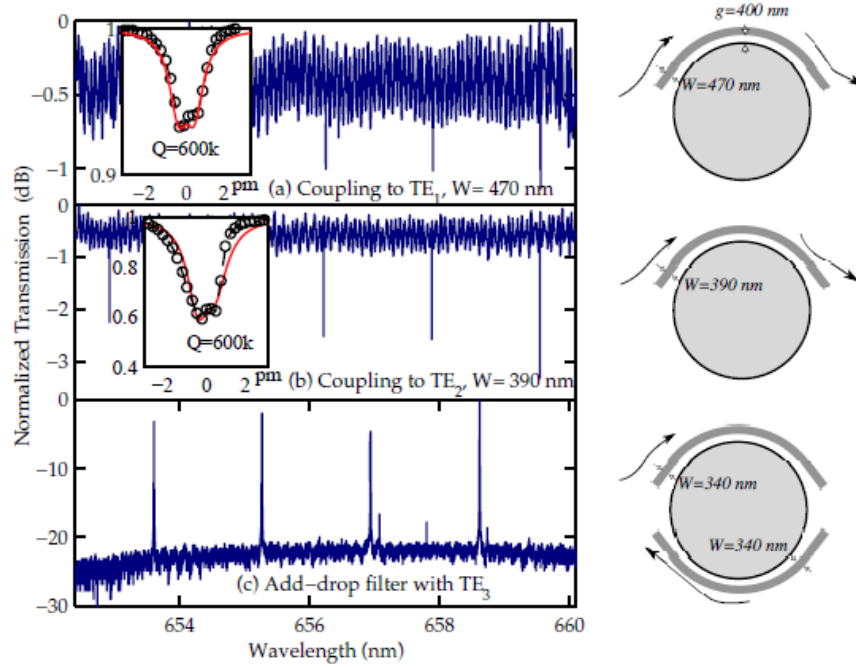


Fig. 15. The normalized transmission of a single-mode, curved waveguide coupled to a microdisk with radius $R = 20 \mu\text{m}$ in the pulley configuration as shown in Fig. 12(a). The coupling length is $l = 30 \mu\text{m}$, and the coupling gap is 400 nm: (a) coupling to the first order microdisk TE mode with $W = 470$ nm; and (b) coupling to the second order microdisk TE mode with $W = 390$ nm. As the waveguide width is reduced, the effective index of the guided mode is reduced, thus higher order resonator modes are phase-matched to the waveguide. (c) The transmission spectrum of the drop port in an add-drop filter with both waveguides being 340 nm wide. Power is transferred to the drop port only when the third radial order TE mode of the microdisk is resonant.

II.B Planar photonic crystal microspectrometers in silicon-nitride for the visible range

Development of the required components in SiN to form a complete sensing system is the next step in the path to capacitate these systems to address major demands of different sensing

applications. Spectrometers, which enable spectral analysis and detection of spectral emission and absorption features, are one of the essential building blocks required to implement the systems needed for many sensing applications. While conventional sensing approaches rely on using bulky off-chip spectrometers, the need for compact mobile or handheld structures has motivated extensive recent progress in the development of integrated on-chip microspectrometers [5].

Several approaches to realize compact spectrometers in the visible range have been proposed previously, including off-chip separation of wavelengths [6], grating spectrometers in low index contrast material [7], frequency-selective detection of light [8], polymer-based implementation [9], and integrated optical spectrometers [10]. However, all these approaches require large structures and offer limited spectral resolution. The focus of this paper is to use the relatively large index contrast in SiN on SiO₂ (through fabricating strongly dispersive photonic crystals) to demonstrate the potential for realizing high-resolution integrated photonic spectrometers with a very small footprint in the visible wavelength range (around 656 nm). The availability of compact spectrometers enables new sensing mechanisms (e.g., monitoring fluorescence and Raman spectra) and new sensing architectures (e.g., multiplexing several resonators for parallel sensing) [4] in the visible integrated photonic systems. The potential integration of silicon detectors and electronic processing units in a compatible platform with SiN sensing components offers a unique prospective for the future of such modules for low-cost, compact, sensitive, and portable sensing applications.

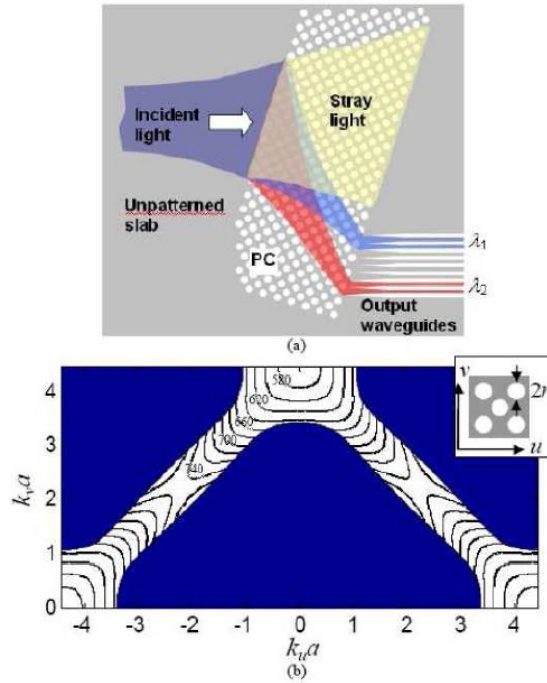


Fig. 16. (a) Schematic visualization of the wavelength separation in a focusing superprism photonic crystal spectrometer is shown. (b) Band structure of a 45°-rotated square lattice planar photonic crystal in SiN on oxide, with holes of 85 nm radius and a lattice constant of 240 nm is shown. Numbers on each contour are the corresponding wavelength for that contour. The shaded regions exclude the modes that leak to the substrate and are not confined to the SiN layer slab. The inset shows the relative direction of the lattice with respect to the principal lattice directions.

Implementation of compact on-chip spectrometers naturally require a mechanism to differentiate between the wavelengths of the input light. This differentiation may occur in a

lumped element (e.g., at an interface) as in grating spectrometers [11], using the dispersion of a set of waveguides as in arrayed waveguide gratings [12], or through propagation in a dispersive material as in superprism-based devices [13]. It is clear that employing stronger dispersion in all these cases results in more compact high-resolution devices. Here, we use the superprism effect in photonic crystals as the main mechanism to achieve spatial spectral mapping in the spectrometer. We follow the basic principle used in silicon-based focusing superprism wavelength demultiplexers [14] to realize compact devices in SiN. The operation concept is based on combining the superprism effect, the negative diffraction effect, and the negative refraction effect inside a photonic crystal structure. The overall configuration is schematically visualized in Fig. 16(a), in which different wavelengths are separated inside the photonic crystal region. In this approach, the angular dispersion inside the photonic crystal is used to steer different wavelengths in different directions inside the structure. At the same time, the negative diffraction property is used to focus the (initially broadened) beam into small spots at the output to make the overall device compact, and the negative refraction is employed to separate the signal of interest from unwanted stray light [14]. It can be observed that the in-plane band structure of the first TE-like mode (i.e., electric field inside the plane of periodicity of the photonic crystal) of a 45° -rotated square lattice photonic crystal, as shown in Fig. 16(a), satisfies all the requirements for achieving superprism, negative diffraction, and negative refraction simultaneously. This band structure is calculated using a three-dimensional plane wave expansion method (based on a supercell) considering the finite thickness of the SiN slab (205 nm). The diameter of holes in this simulation is 170 nm, and the lattice constant is 240 nm. As it can be seen from Fig. 16(b), in this structure there is an operation range below the light line that shows strong dispersion effects while demonstrating simultaneous negative diffraction and negative refraction. To explore the extent of strong dispersion in this structure, we can also consider higher photonic bands of the planar photonic crystal [15]; however, because of the limited contrast between the SiN layer and the underneath SiO_2 layer, higher photonic bands of this planar structure are not confined to the slab anymore.

To find the optimal device parameters, we use the envelope transfer function [16] to approximately model the beam propagation inside the photonic crystal region. The configuration of the structure used in this modeling is shown in Fig. 17(a). The input beam is incident on the photonic crystal interface from an unpatterned slab region (to simulate the operation of the actual device) at an incident angle of 13° in this case. The beam undergoes some diffractive broadening prior to entering the photonic crystal region, such that the overall second-order diffraction is canceled at the output of the device at the center wavelength of 656 nm. The width of the photonic crystal region is $L = 70 \mu\text{m}$, and it has a 45° -rotated square lattice with lattice constant $a = 240 \text{ nm}$ and hole diameter $2r = 170 \text{ nm}$. Fig. 17(b) shows the simulated intensity of the beam at the output of the photonic crystal region at three different wavelengths. The separation of adjacent wavelength channels with wavelength difference $\Delta\lambda = 2.4 \text{ nm}$ is evident from Fig. 17(b). For this structure, two non-idealities determine the crosstalk between these wavelength channels: (1) relatively strong side-lobes in the intensity profile introduced by the third-order diffraction effect in these structures [17], and (2) second-order broadening at wavelengths away from the center wavelength of operation. These effects degrade the cross-talk isolation level from potentially higher than 12 dB (for non-distorted Gaussian beams with 2.4 nm spacing in the same structure) to around 6 dB. Fig. 17(c) shows the effect of changing the width of the incoming optical beam in the same structure. Increasing the input beamwidth has two direct effects. On

one hand, it directly increases the spatial extent of the beam at the output (even when the beam is not affected by diffractive broadening); on the other hand, it reduces the effect of both second-order and third-order distortions [17], by reducing the spatial frequency content of the beam. Fig. 17(c) clearly shows both of these effects. The intensity of each plot in Fig. 17(c) is compared to its non-distorted Gaussian case; therefore, lower peak intensity for smaller beamwidths in this figure is an indication of more diffractive broadening. The optimal beamwidth, $2w_0$, can be determined by considering the trade-off between the original extent of the beam and its diffractive broadening inside the structure. In this particular design, we have chosen $2w_0 = 4 \mu\text{m}$ as the waist of the input beam.

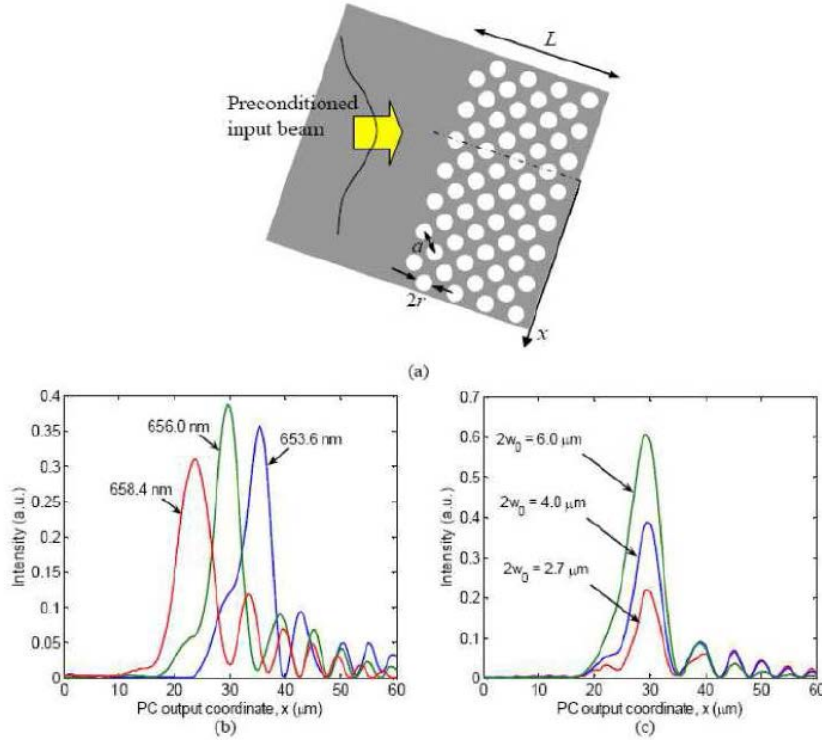


Fig. 17. (a) The configuration used for the simulation of optical beam propagation in a SiN PC is shown. A 45° -rotated square lattice photonic crystal with $L = 70 \mu\text{m}$, $2r = 170 \text{ nm}$, $a = 240 \text{ nm}$ is assumed. The thickness of the SiN slab is 205 nm , the incident angle is 13° , and the light has TE-like polarization. (b) Output beam profiles at different wavelengths (653.6 nm , 656.0 nm , and 658.4 nm) for input beam waist of $2w_0 = 4 \mu\text{m}$ are plotted. The input beam is preconditioned to compensate the effect of second-order diffraction at 656 nm . (c) For the same structure as in part (b), output beam profiles at different input beam waists of $2w_0 = 2.7, 4.0$, and $6.0 \mu\text{m}$ are shown.

To experimentally demonstrate the operation of these SiN spectrometer devices, we have used standard microelectronic fabrication facilities to pattern the planar SiN slab [18]. The process consists of electron-beam lithography (EBL) followed by CF_4 -based inductively coupled plasma (ICP) etching to transfer the desired pattern into the wafer. The stoichiometric SiN wafer used in our fabrication has a 205 nm ($\pm 5 \text{ nm}$) thick SiN device layer deposited on $6 \mu\text{m}$ of thermally grown silicon dioxide (SiO_2). The SiO_2 layer completely isolates the light in the device layer from the lossy silicon substrate. Fig. 18(a) shows the scanning electron microscope (SEM) image of the fabricated structure consisting of a photonic crystal region, similar to the configuration in Fig. 18(a), and an array of waveguides at the output to spatially sample the beam

profile and carry it to the output edge of the sample. Fig. 18(b) shows the details of the photonic crystal structure fabricated in SiN. The input waveguide is then tapered up to $4\ \mu\text{m}$, and is then terminated to an unpatterned SiN slab to launch the incident beam to the photonic crystal region. To precondition the beam, the input beam propagates and diffracts in the unpatterned SiN slab region before reaching the photonic crystal region [14]. The length of the preconditioning region in this structure is $1.1\ \text{mm}$; however, note that this length does not impose an intrinsic limit on the compactness of the structure, since, for example, it can be replaced by a curved mirror [20]. After passing through the photonic crystal, the output light from the photonic crystal region is coupled into an array of output waveguides with $3\ \mu\text{m}$ spacing. The signal in these output waveguides is measured by imaging the output facet onto a single detector (using a $20\times$ objective lens at the output). The signal from individual output waveguides is isolated using an iris and measured while the tunable laser scans the wavelength. Fig. 19(a) shows the measured power in seven of the output waveguides that fall within the range of the available tunable laser.

From the measurement results in Fig. 19(a), we mark the wavelength of the peak of the beam intensity at each output and deduce the angular dispersion of the photonic crystal structure. Fig. 19(b) shows the angle of refraction found from the measurement (solid line) and compares it with the estimated angle of refraction from the theoretical model (dotted line, based on the band structure calculations in Fig. 16). It can be seen that the measured dispersion matches the theoretical expectations closely. From Fig. 19(b) it can be observed that the device is operating in the negative refraction regime (as designed), and the angle of refraction changes rapidly with wavelength (strong superprism effect). Considering the $3\ \mu\text{m}$ spacing between the adjacent output waveguides, the extent of the output beam intensity at each wavelength can be estimated from Fig. 19(a) to be around $5\ \mu\text{m}$. By comparing this beam extent with the initial beam waist ($\sim 4\ \mu\text{m}$) and the beamwidth at the input plane of the photonic crystal region ($\sim 80\ \mu\text{m}$), we can readily see that the device is working in the negative diffraction regime. These observations confirm the operation of the fabricated device in the desired operation regime. This fabricated device shows spatial separation of different wavelength channels with around $1.2\ \text{nm}$ wavelength resolution in a $70\ \mu\text{m} \times 130\ \mu\text{m}$ photonic crystal structure.

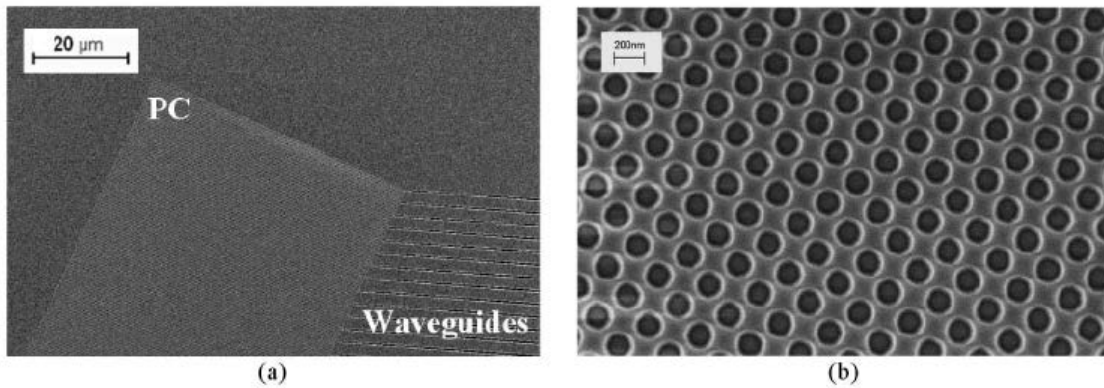


Fig. 18. (a) SEM image of the fabricated structure is shown with a rotated PC region and an array of waveguides at the output. The incident beam is directed from a tapered waveguide from the left side of the device at an incident angle of 13° with respect to the interface of the photonic crystal region. (b) SEM image of the details of the photonic crystal region is shown. From SEM images, the lattice constant in the fabricated device is $a = 240\ \text{nm}$, and the diameter of holes is $168\ \text{nm}$ (compared to the $170\ \text{nm}$ designed value).

To further validate the operation of the device, we have simulated the propagation of optical beams at different wavelengths in a photonic crystal structure with the parameters similar to our

fabricated device. Note that the actual parameters of the fabricated device are slightly different from the design values because of the limited accuracy of the fabrication process. We have employed the in-plane band structure of the planar photonic crystal (calculated using a three-dimensional plane wave expansion method) and the envelope transfer function [16] to calculate the output beam intensity at different wavelengths (similar to what we did to obtain the results shown in Fig. 17). By integrating the beam power over $\sim 3 \mu\text{m}$ intervals (i.e., the acceptance range of each output waveguide) at the output plane of the photonic crystal region, the channel responses (at output waveguides) is found. Figure 20 shows the calculated channel responses calculated with the same waveguide positions and spacing as the fabricated structure. By comparing Fig. 20 with Fig. 19(a), we can observe that the theoretical estimates and experimental results of the spatial extent of the beam and the level of side-lobes are in good agreement. Thus, we expect this theoretical model to accurately represent the performance of such spectrometers in future designs and perform as a reliable tool for estimating the spectral resolution and the isolation level.

There are three major criteria for evaluating the performance of spectrometer devices and configurations: compactness, spectral resolution, and insertion loss. These parameters determine how well the spectrometer can perform in different applications, e.g., as a spectral analysis unit in a sensing platform or as a wavelength demultiplexer in an optical information processing system. The use of strong dispersion in photonic crystals provides the potential to implement a high resolution device in a small footprint. From Fig. 19(b), an angular dispersion factor (i.e., change in angle as a function of wavelength) of $2.3^\circ/\text{nm}$ is observed, which is much larger than $0.17^\circ/\text{nm}$ achievable in a conventional grating spectrometer realized in the same platform. This large angular dispersion factor further confirms the size advantage of the superprism-based photonic crystal spectrometers over alternative implementations. The angular dispersion in this device is almost twice as high as previous demonstration of the superprism effect in silicon nitride [19]. Furthermore, combining the superprism effect with the diffraction compensation scheme significantly improves the spatial separation (in a similar size) compared to the brute-force angular separation scheme (with diverging optical beams) in previous works [19]. Note that the structures shown in this work, which are optimized for compactness and high spectral resolution, are not necessarily the optimal designs in terms of insertion loss. We have observed less than 8 dB insertion loss (defined as total output power divided by total input power) in the device shown in Fig. 19. This insertion loss value is estimated by comparing the output power from all the output channels of the spectrometer with the power in a ridge waveguide fabricated on the same substrate and is accurate within ± 1 dB (due to the limitations of our characterization setup). A considerable portion of the loss (> 4 dB) in the demonstrated photonic crystal spectrometer is caused by the choice of excitation of the structure using a terminated waveguide in the far-field. This loss can be significantly reduced by using a mirror with proper curvature as the preconditioning region at the input of the structure [20]. Further reduction of loss can be achieved by modifying the interface of the structure and by including matching stages [21, 22] to reduce the scattering and reflection losses when coupling the light into and out of the photonic crystal region. Furthermore, more elaborate fabrication processes, such as deep anisotropic etching the SiO_2 layer underneath the SiN layer or undercutting the structure by wet etching can be used to further reduce the loss in the structure. We expect to considerably reduce this insertion loss by considering all these factors in the design and fabrication of these planar photonic crystal spectrometers.

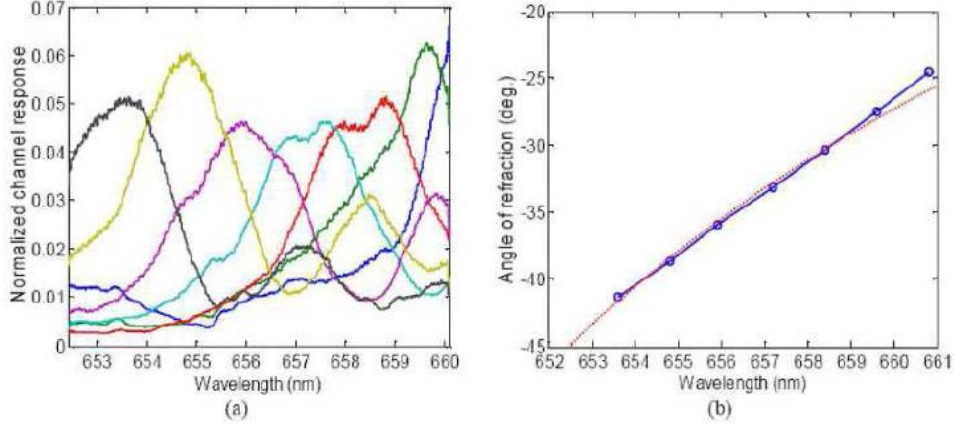


Fig. 19. (a) Measured normalized transmission responses in adjacent channels are shown for seven output waveguides, showing a 3-dB wavelength resolution less than 1.2 nm. (b) The experimentally measured angle of refraction (solid curve) is shown and compared with theoretical prediction (dotted line). Theoretical results are corrected by a wavelength shift of 1.1% that accounts for the deviations of the thickness of the SiN slab and the size of holes from the designed values.

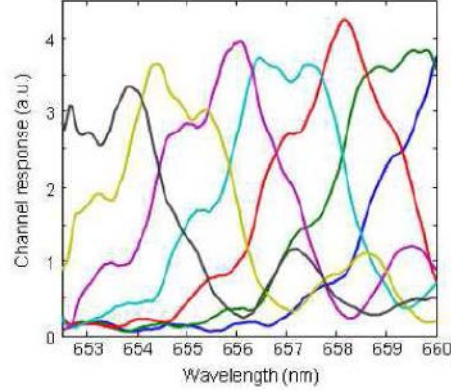


Fig. 20. Simulated channel responses of optical beams at different wavelengths (calculated at 50 pm wavelength steps) in a planar photonic crystal spectrometer are shown. All the parameters of the simulated structure are similar to the fabricated structure in Fig. 17. Similar to Fig. 19(b), the theoretical results are corrected by a wavelength shift of 1.1% to account for the deviations of the fabricated structure from the designed values. The simulated channel response for each output waveguide in these results is in good agreement with the experimental measurements in Fig. 19(a).

To compare the performance of the demonstrated spectrometer with the alternative implementations, we have fabricated spectrometers based on different operation principles on the same substrate. The structures being compared here are (1) the photonic crystal spectrometer studied earlier in this paper; (2) an arrayed waveguide grating (AWG) made by following the standard design in [23]; (3) the same AWG as in (2) after a resist reflow process [24] to reduce the sidewall roughness and reduce the waveguide propagation loss; and (4) a folded grating spectrometer operating in the first-order reflection grating mode [25]. All these devices are designed to have small footprints, and are fabricated in our group with the same fabrication recipe. The SEM images of these fabricated structures are shown in Fig. 20. To characterize the performance of each device, we have used the same measurement setup explained in Section 3. The resolution of each spectrometer is measured by scanning the wavelength of the input laser and measuring the power at each output waveguide. The insertion loss is also measured by comparing the total output power of the device with that of a straight waveguide fabricated on the same substrate. The performance of the devices, shown in Table 1, are compared using two

main metrics: (1) compactness factor, $C_\lambda = [l_p(\Delta\lambda)_{3dB}]^{-1}$, where l_p is the length scale of the device and $(\Delta\lambda)_{3dB}$ is the spectrometer full-width half maximum wavelength resolution, and (2) insertion loss of the spectrometer. The compactness factor provides a measure that for a given wavelength resolution how compact each device is, and the insertion loss is the drop in the signal level while passing through the spectrometer. Note that in some practical situations, e.g., in a sensing platform [4], higher signal-to-noise ratio at the output can be traded in favor of an effectively higher detectable wavelength resolution. Therefore, we can use the power-normalized compactness factor, C_λ / IL (listed in the last column of Table 1), as the main spectrometer comparison criteria. It can be observed that among these compact implementations, the photonic crystal spectrometer shows favorable performance even without employing further loss-reduction solutions. Note that this comparison between different device implementations cannot be viewed as an absolute measure for performance of such structures. All the different spectrometers demonstrated here have been designed with compactness as one of the major factors, and can be further optimized for better resolution and lower insertion loss. Nevertheless, the preliminary comparison of the performance of these structures under similar fabrication quality as presented in Table 1 provides a point of reference for future optimization of these devices. In our view, the compactness and insertion loss of the spectrometers as mentioned in Table 1, should be directly included in the performance measure of the device for future integrated spectrometer optimizations.

Note that the operation range in the devices used in this paper is located at the crossing of the zeroth order and the first-order bands of the photonic crystal [26]. The modes in this operation region are hybrid modes mainly consisting of the zeroth order and first-order Bloch components. The transition of the dominant component from the zeroth order component to the first-order component is the main factor in the rapid change in the direction of propagation of the hybrid mode (and therefore, a strong superprism effect). In low-contrast SiN photonic crystal structures, compared to high contrast platforms such as silicon-on-insulator (SOI), the coupling between the zeroth order and the first-order components is weaker. This weaker coupling manifests itself in smaller available bandwidth and more higher-order diffractive distortion (and thus, lower cross-talk isolation) in spectrometer devices made in the low-contrast SiN photonic crystals. The higher-order diffraction effects distort the optical beam shape at the output of the device and causes relatively large channel-to-channel cross-talk in these spectrometers. In principle, a multistage photonic crystal structure can be used to provide more degrees of freedom to control the beam shape and reduce the cross-talk. Currently, the applicability of this multistage scheme is, however, limited by the required fabrication accuracy in different regions of such multistage structure.

The limited available operation bandwidth (around 10 nm) of the demonstrated SiN photonic crystal spectrometer (for example, compared to AWGs in which the operation bandwidth is easily scalable) is one of the shortcomings of the proposed scheme. However, the useful bandwidth of the photonic crystal spectrometer can be extended by using a cascaded scheme with a coarse wavelength demultiplexer in the first stage followed by compact high-resolution photonic crystal spectrometers to cover different bands.

Table 1. The performances of SiN spectrometers based on different operation principles are compared.

	Compactness factor, C_λ (nm.mm) ⁻¹	Insertion loss, IL (dB)	C_λ/IL (nm.mm) ⁻¹
Photonic crystal	7.0	8.0	1.1
AWG-reflow	2.8	6.5	0.63
AWG	2.8	11	0.22
Grating-based	1.1	8.0	0.17

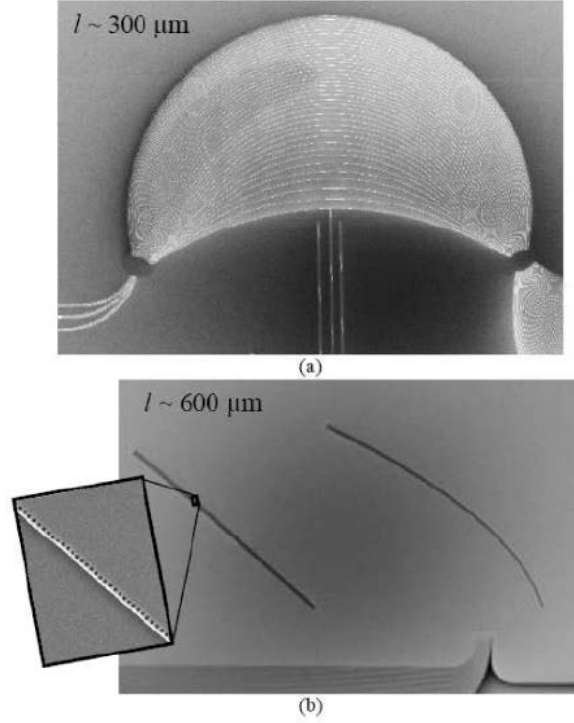


Fig. 21. SEM images of alternative on-chip spectrometers implemented in SiN for comparison of spectroscopy performance are shown. (a) An AWG spectrometer with a size-scale of $l = 300 \mu\text{m}$ and wavelength resolution of 1.2 nm. (b) A folded grating spectrometer with a size-scale of $l = 600 \mu\text{m}$ and wavelength resolution of 1.5 nm. The inset magnifies a portion of the grating reflector that consists of a periodic pattern of air holes next to a wide trench [25].

In summary, we have shown the potentials of planar photonic crystal devices as on-chip spectrometers in SiN. The demonstrated structures offer exceptional compactness and high spectral resolution performance as integrated components. A 3-dB spectral resolution of 1.2 nm and less than 8 dB insertion loss are experimentally observed in the $70 \mu\text{m}$ by $130 \mu\text{m}$ photonic crystal structure investigated in this work. It is shown that the demonstrated superprism-based photonic crystal spectrometers even without further optimization are advantageous over other compact implementations of spectrometers in SiN. Future steps to reduce the insertion loss in these devices are expected to further improve their performance.

II.C Athermal photonic devices

II.C.1 Athermal polymer-clad Si high Q microresonators

The refractive index of Si is strongly temperature dependent. The dn/dT , which is called the thermo-optic coefficient (TOC), is $+1.8 \times 10^{-4} \text{ K}^{-1}$ in Si, and for a typical microdisk resonator the resonance wavelength changes $+78 \text{ pm/K}$ at 1550 nm (radius $\sim 10 \mu\text{m}$ and thickness $\sim 220 \text{ nm}$) and for a microring resonator the resonance wavelength changes $+66 \text{ pm/K}$ (radius $\sim 10 \mu\text{m}$ and a $500 \times 220 \text{ nm}^2$ cross-section). However, in several important applications of photonic integrated circuit applications (e.g. delay lines, narrow-band filters), a stable resonance property is a key requirement. Hence, athermal operation of such Si high Q microresonators becomes a critical requirement. Using the closed form expression for the resonance condition in a TWR we can show that athermal performance is achieved when the two thermo-optic effects (in core and cladding) completely cancel each other, i.e., when

$$\frac{n_{\text{clad}} \frac{dn_{\text{clad}}}{dT}}{n_{\text{core}} \frac{dn_{\text{core}}}{dT}} = -\frac{\Gamma}{1-\Gamma}. \quad (6.5)$$

where we define Γ as the mode confinement factor. It can be seen from Eq. (6.5) that realizing athermal operation in a device with a higher confinement demands a cladding material with a larger negative TOC. Si-based TWRs are typically high-confinement devices; this, in addition to the large TOC of Si, and the fact that the TOC of polymers is usually smaller than $-5 \times 10^{-4} \text{ K}^{-1}$, means that using a large-TOC polymer is often not sufficient for full compensation.

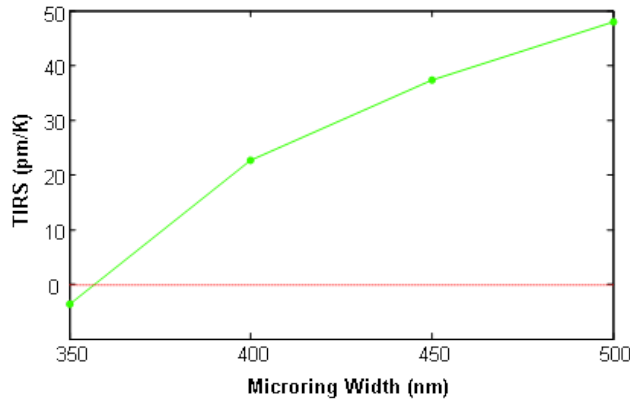


Figure 22. Simulation results for the thermally-induced resonance shift at 1550 nm as a function of the resonator width, in a PUA-clad $10\text{-}\mu\text{m}$ -radius microring resonator. The thickness of the Si layer is 220 nm .

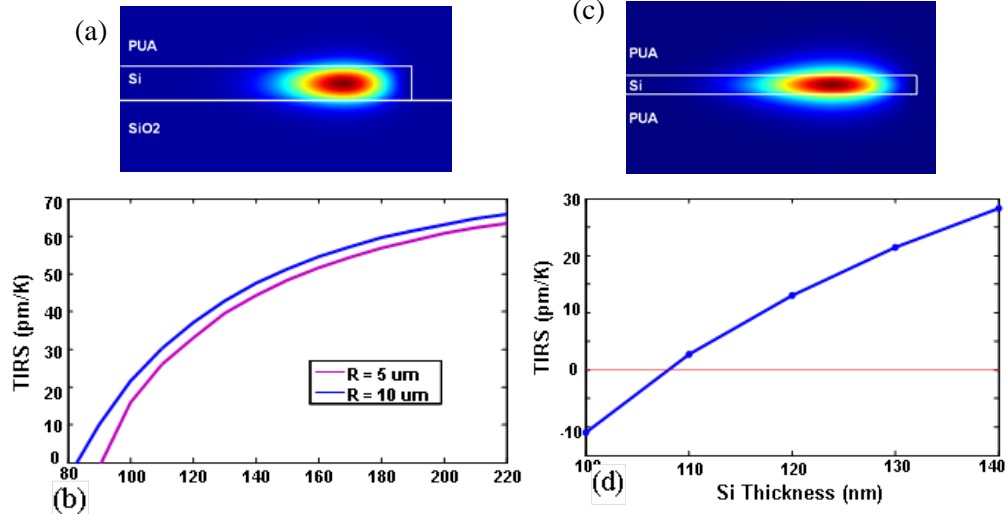


Figure 23. (a) Cross-sectional plot of the fundamental TE mode for a PUA-clad microdisk resonator with a radius of 10 μm and a thickness of 220 nm. (b) Simulation results for the thermally-induced resonance shift at 1550 nm, in PUA-clad microdisk resonators with various thicknesses and radii. The results are shown for the fundamental TE mode. (c) Cross-sectional plot of the fundamental TE mode for a PUA-clad undercut microdisk resonator with a radius of 10 μm and a thickness of 110 nm. (d) Simulation results for the TIRS at 1450 nm versus the Si layer thickness, in a PUA-clad 10- μm -radius undercut microdisk resonator. The results are shown for the fundamental TE mode.

During this period of the PECASE program, we have explored two ways to achieve athermal operation in high-Q high-confinement Si microresonators (i) the use of athermal polymers with high TOC and (ii) the use of novel device designs to achieve athermal operation. For the negative TOC, we have explored the use of an aliphatic polyester-based urethane diacrylate polymer (PUA), with a measured TOC of $-4.5 \times 10^{-4} \text{ K}^{-1}$, which is, to our knowledge, one of the largest TOCs in polymers. The refractive index of PUA is about 1.45. We use a finite element method (FEM) mode solver to calculate the thermally-induced resonance shift (TIRS) in microresonators with various sizes. Figure 22 shows the TIRS as a function of the resonator width for a 10 μm radius 220-nm-thick PUA-clad microring with athermal operation achieved for a width ~ 350 nm. For a Si microdisk, we find that changing the Si layer thickness affects TIRS much stronger than when changing the resonator radius. Zero TIRS is achieved in Si microdisks at thicknesses of about 80 nm and 90 nm, respectively, for resonator radii of 10 μm and 5 μm . Another geometry we have studied is the undercut geometry. This should increase the percentage of the mode field that interacts with the negative TOC polymer. This could be achieved by removing the buried oxide (BOX) layer around the edge of the microdisk and filling this space underneath the resonator with the polymer. Figure 23 shows the calculated TIRS against the Si layer thickness in a 10- μm -radius PUA-clad undercut geometry (results shown for the fundamental TE mode). The TIRS is close to zero for a Si device layer thickness of 110 nm.

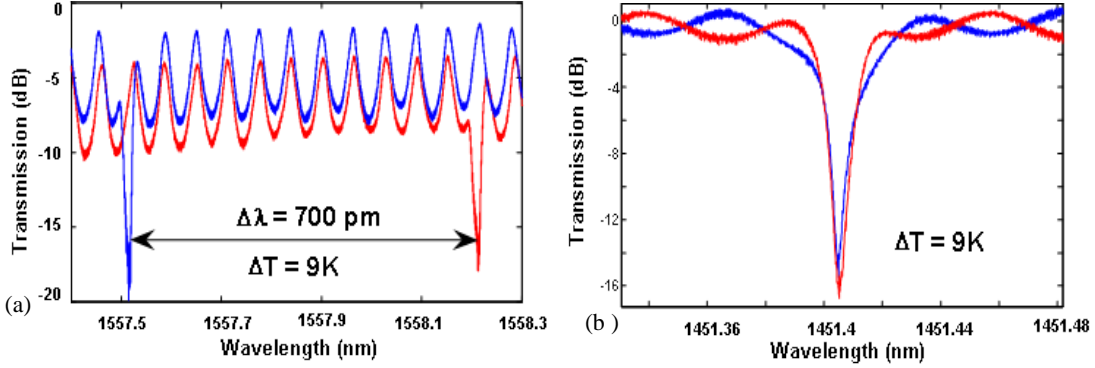


Figure 24. (a) Thermally-induced resonance shift in a 10- μm -radius 220-nm-thick microdisk without any compensation effort. (b) Athermal resonance in a 10- μm -radius 110-nm-thick PUA-clad undercut microdisk.

In order to confirm our designs and simulations, we have fabricated undercut high-Q Si microdisk resonators and covered them with the negative TOC polymer. During the TIRS measurements, the samples are placed on a TEC-equipped stage with a built-in thermistor to monitor the temperature. The transmission spectra are measured before and after increasing the temperature. Two cases are shown in figures 24(a) and 24(b): the first one belongs to a 10 μm radius, 220-nm-thick microdisk without any cladding, exhibiting a large resonance shift (78 pm/K); the second one is related to a PUA-clad 10 μm radius undercut microdisk with a device layer of 110 nm, which is close to the predicted optimum. We experimentally observed nearly athermal performance (TIRS ~ 0.2 pm/K). The close agreement with the theoretical calculations, suggest that the polymer was able to completely fill the space underneath the resonator. These initial results suggest that with careful and optimized device designs, athermal high-Q microresonators are achievable in the Si platform. Such athermal high Q Si microdisk resonator devices could be useful for several applications where stable resonance frequencies are critical (e.g. delay lines, narrowband filters).

II.C.2 Titania-Clad Microresonators on SOI

Travelling-wave resonators (TWRs) on silicon-on-insulator (SOI) platform have found numerous applications in the field of silicon photonics, because of their high Q-factors and small mode volumes, as well as design simplicity and mechanical stability. They have been utilized to implement filters, spectrometers, modulators, and various other functionalities needed in Photonic Integrated Circuits (PICs).

One of the main issues of silicon-based PIC is the strong temperature dependence of the refractive index of silicon. The thermo-optic coefficient (TOC) of Si is $+1.8 \times 10^{-4} \text{ K}^{-1}$; consequently, TWRs made of Si are highly temperature-sensitive. For a typical microring with a radius of 10 μm and a cross-section of $450 \times 220 \text{ nm}^2$, the thermally-induced shift in the resonance wavelength is about 75 pm/K (or equivalently, $\sim 10 \text{ GHz/K}$) at 1550 nm. As a result, the fluctuations in the ambient temperature, and the temperature variations across the chip, pose a problem for applications that rely on stable resonance properties, such as delay lines and narrow-band filters. It is therefore desirable to reduce the temperature sensitivity of these resonators as much as possible.

One of the methods used to achieve this goal is to coat the resonators with some type of polymer. The negative TOC of polymers is used to compensate the positive TOC of the Si core. Ultimately, the magnitude of the thermal shift is a function of the polymer TOC and the

confinement of the resonant mode. Athermal microrings [27] and microdisks [28] have been demonstrated using this method.

The negative TOC of polymers is a result of the thermal expansion effect, which leads to a reduction in the number of dipoles per unit volume, and consequently, the refractive index. Some polymers have TOCs as large as $-5 \times 10^{-4} \text{ K}^{-1}$, which is very useful for athermal design. However, a major drawback is the fact that most polymers have a low heat resistance, and therefore, are not CMOS-compatible.

The thermo-optic effect in inorganic materials is generally dominated by the increase of polarizability, which results in a higher refractive index and therefore, a positive TOC. However, titanium dioxide (TiO_2 , commonly called titania) is an exception because of its large negative TOC (a function of wavelength, temperature, and deposition process) [29]. It also has a high refractive index (over 2, and strongly dependent on the method of deposition) that pulls the optical mode toward the cladding. The combination of the large TOC and the high index can significantly reduce the temperature sensitivity of the titania-clad device. Titania has a very high melting point (1840°C). Titania thin films are extensively used in the optics industry, and the related technology is well-developed. The CMOS compatibility of titania makes it an excellent choice for integrated applications.

For this work, we have used electron-beam evaporation for the deposition of titania. The as-deposited titania is amorphous, and we measured its refractive index to be 2.02 at the 1550 nm wavelength. We fabricated a series of microrings with varying widths on an SOI wafer with a 220-nm-thick top layer. The patterns were written by electron-beam lithography on ZEP electron-beam resist with a dose of $280 \mu\text{C}/\text{cm}^2$. Etching was done using inductively-coupled chlorine plasma. Finally, titania was deposited on top of the devices through electron-beam evaporation. An SEM image of a microring resonator is shown in Fig. 25(a).

The samples were placed on a TEC-equipped stage, and tapered fibers were used to couple light into and out of the bus waveguides. The transmission spectra were obtained before and after changing the temperature. Fig. 26(a) shows the transmission spectra of a $10\text{-}\mu\text{m}$ -radius, $450 \times 220 \text{ nm}^2$ microring, before and after a 10 degree temperature rise. The resonance shift at 1570 nm is about -18.6 pm/K , suggesting that the microring is overcompensated.

We use a finite element method (FEM) mode solver to simulate the thermo-optic shift of resonance in microrings. Fig. 25(b) shows the cross-sectional profile of optical power in a titania-clad microring resonator with a radius of $10 \mu\text{m}$ and a cross-section of $450 \times 220 \text{ nm}^2$. Based on our simulations, the measurement result corresponds to a TOC of $-6.7 \times 10^{-4} \text{ K}^{-1}$ at the 1570 nm wavelength. Fig. 25(c) shows the simulation results for the thermally-induced shift at 1570 nm in microrings with different widths, using $-6.7 \times 10^{-4} \text{ K}^{-1}$ for the TOC of titania. We expect from Fig. 25(c) for the 500-nm-wide ring to be athermal (i.e., the resonance shift is close to zero). Fig. 26(b) shows the transmission spectra of a $500 \times 220 \text{ nm}^2$ microring, before and after a 10 degree temperature rise. It can be seen that the resonance is athermal; therefore, the results are in agreement with our simulations.

The intrinsic Q-factors of the microrings were around 75,000, which is not different from the value that we get without the titania cladding. This means that the titania cladding does not create a source of major optical loss.

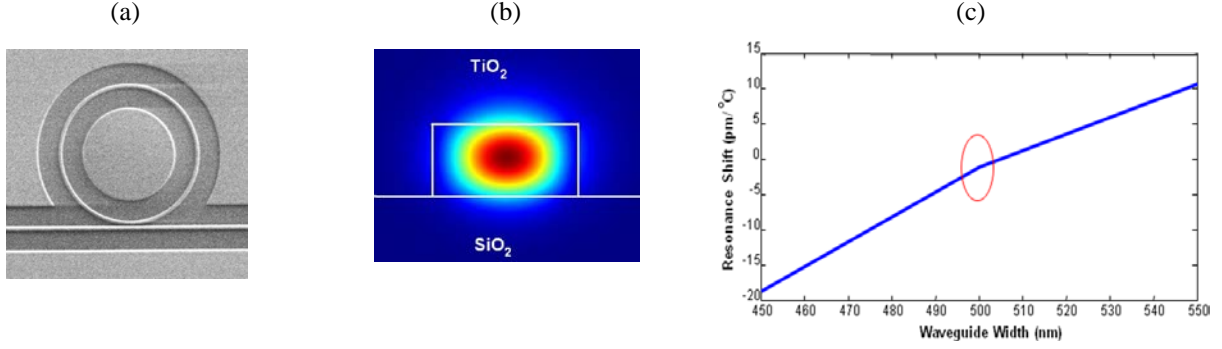


Fig. 25. (a) SEM image of a microring resonator. (b) Cross-sectional mode profile of a $450 \times 220 \text{ nm}^2$ titania-clad microring resonator with a radius of $10 \text{ } \mu\text{m}$. (c) Simulation results for thermally-induced resonance shift in microrings with different widths (height 220 nm).

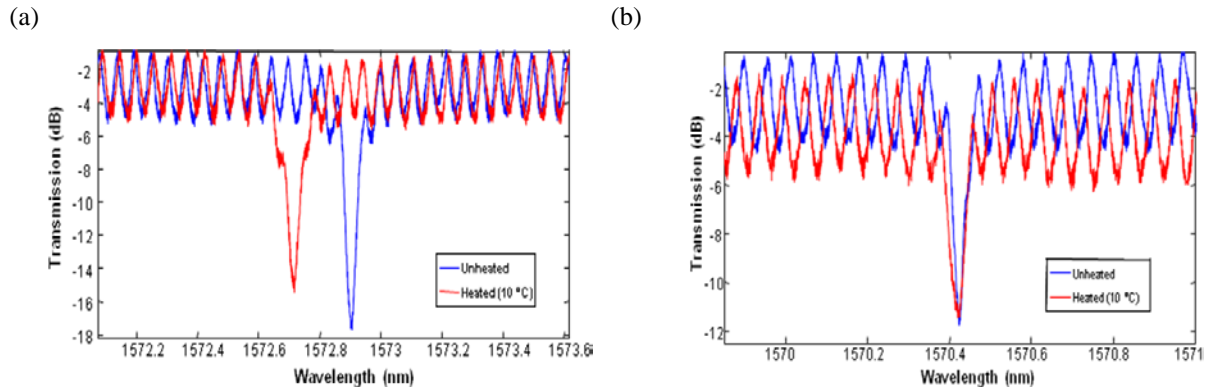


Fig. 26. (a) Resonance shift in a $450 \times 220 \text{ nm}^2$ titania-clad microring at 1570 nm (b) Athermal resonance in a $500 \times 220 \text{ nm}^2$ titania-clad microring at the same wavelength.

II.C.3 A temperature-insensitive third-order coupled-resonator filter for on-chip terabit/s optical interconnects

The trend toward multicore architectures and chip multiprocessors requires power-efficient on-chip interconnects with terabit/s (Tb/s) capacity to facilitate information exchange among cores and the external memories [30-32]. While conventional electrical interconnects approaching Tb/s aggregate bandwidths have been achieved [30], there has been a major research thrust in recent years to realize integrated photonic architectures for the future applications requiring hundreds of cores running independently while shuttling data back-and-forth [30-32]. The major advantages offered by photonics are the low energy required to transmit the information and the potential for wavelength-division multiplexing (WDM) to enable large increase in the number of connections. A promising recent result uses WDM channels that are simultaneously switched and routed to provide a large aggregate bandwidth with manageable power consumptions [31]. To achieve such a network, one critical element is an optical switch realized using an optical filter capable of accommodating multiple wavelength channels. Also, considering the large temperature fluctuations in a realistic on-chip environment (up to tens of degrees), the optical filter has to be temperature insensitive [32].

In previous studies, both single- and coupled-resonator filter architectures implemented in the silicon-on-insulator (SOI) platform have been reported [32-34]. 20 wavelength channels were

simultaneously switched using a single microring resonator [33]. However, since the filter channels are narrowband (3dB bandwidth ~ 0.1 nm), small temperature shifts can easily cause the wavelength registration problem. To solve this issue, coupled-resonator structures with large bandwidth filter channels were utilized to provide extra thermal guard band [32, 34]. However, these coupled-resonator filters suffered from large free-spectral-range (FSR), which makes scalability to large WDM channel counts challenging. As a result, only 9 and 3 WDM channels were reported in [32] and [34], respectively.

In this report, we show temperature-insensitive filters utilizing resonators with smaller FSR, which allows a more manageable optical bandwidth. The adverse effect of small FSR is the proportional reduction of the individual filter channel bandwidths, resulting in insufficient thermal guard band. Here we show that by employment of a negative thermo-optic coefficient (TOC) polymer overlay on the silicon device layer, the temperature dependence of the filter can be significantly reduced, and temperature-insensitive performance is thereby achieved.

Device Design

The structure investigated in this letter is a symmetric third-order coupled-resonator filter as shown in Fig. 27(a), where κ_0^2 , κ_1^2 denote the power coupling ratios between the end resonator and the access waveguide and that between the adjacent resonators. In order to minimize the impact of the strong material dispersion of silicon, the FSR of the filter has to be as small as possible. Since the target 3-dB bandwidths of filter channels are on the order of 1 nm to accommodate wideband wavelength channels (e.g., 100 Gb/s), an FSR around 5 nm is empirically found appropriate to provide the necessary bandwidth and adequate channel isolation. To obtain a flat-band response, κ_0^2 and κ_1^2 have to satisfy certain relationships. For example, in the narrowband filter design, $\kappa_1^2/\kappa_0^4 \approx 1/8$ is required while in the wideband filter design the exact ratio of κ_1^2/κ_0^4 may be different [34]. Therefore, for flat-band design, κ_0^4 and κ_1^2 should follow a similar wavelength dispersion curve.

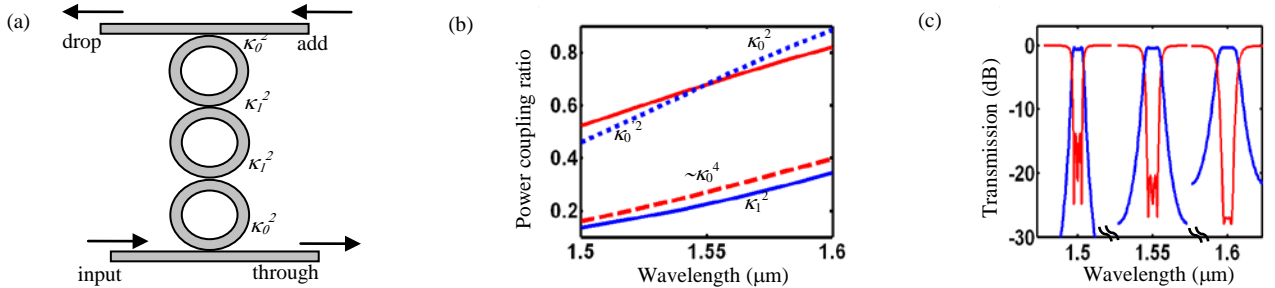


Fig. 27. (a) Schematic of the third-order filter; (b) power coupling ratios of the synchronous parallel waveguide couplers with different gaps and coupling lengths: κ_0^2 (gap 160 nm, length 4.4 μm), κ_0^2 (gap 300 nm, length 10.2 μm) and κ_1^2 (gap 300 nm, length 5.2 μm); (c) three simulated filter channel responses with power coupling ratios κ_0^2 and κ_1^2 provided in (b).

In this work, resonators and waveguides are evanescently coupled to each other. The design approach consists of two aspects, the first being the broadband coupling engineering and the second being the temperature insensitive design. Initially, the waveguide dimensions are optimized to fine-tune the thermal property of the filter. We use a waveguide with a height of 144 nm and a width of 425 nm covered with a top polymer cladding to achieve athermal response exactly at 1.5 μm . The choice of this wavelength for the athermal operation will be elaborated later. Since we are targeting multiple filter channels (~ 20) over a wide wavelength

range (~ 100 nm), the resonator's coupling to the access waveguides and the adjacent resonators needs to be optimized to achieve a wideband coupling performance. In this regard, a microring performs significantly better than a racetrack due to its effective shorter coupling length under fixed FSR and power coupling ratio. While a detailed comparison could be performed through 3-dimensional finite-difference time-domain (FDTD) simulations, here we adopt a simpler approach where the coupling region of two coupled structures is modeled by a parallel waveguide coupler with the same gap and an equivalent coupling length [35]. Fig. 27(b) shows the simulation results for the dispersion of the power coupling ratios of a synchronous parallel waveguide coupler (with the mentioned waveguide dimension) for different values of gaps and coupling lengths. The upper two curves correspond to couplers with identical power coupling ratios at $\lambda = 1.55$ μm , but the one with a shorter coupling length exhibits less dispersion over the wavelength range 1.5 μm -1.6 μm . This observation leads us to use microrings with radius of 21 μm (instead of racetracks) for the filter design. Following the procedure outlined in [34] which uses the synchronous parallel-coupler model, the waveguide-resonator and resonator-resonator gaps are found to be 160 nm and 300 nm, resulting in an equivalent coupling length of 4.4 μm and 5.2 μm , respectively. κ_0^2 and κ_1^2 are shown accordingly in Fig. 27(b) by the upper solid line and the lower solid line, respectively. The condition for flat-band response is also verified in Fig. 27(b), where κ_0^4 shows a similar dispersion compared to κ_1^2 . Using these parameters for the device, the overall filter response is obtained through a rigorous matrix analysis [34]. In Fig. 27(c), we show three such filter channels around 1.5 μm , 1.55 μm and 1.6 μm , respectively. From Fig. 27(c), we observe that: 1) filter responses are reasonably good, and flat-band filter channels exhibit more than 15 dB extinction in the through port and more than 20 dB out-of-band rejection in the drop port; 2) the 3-dB bandwidth increases from 0.75 nm at $\lambda = 1.5$ μm to 1.5 nm at $\lambda = 1.6$ μm , primarily due to the material dispersion impacting κ_0^2 and κ_1^2 as seen in Fig. 27(b); 3) the bandwidth of the filter channels increases with wavelength, and the finesse of the filter decreases and consequently, the out-of-band rejection becomes smaller (more than 30 dB at 1.5 μm and only 20 dB at 1.6 μm) ; 4) the through port responses are improved at longer wavelengths, indicating a better impedance match among coupled resonators and the end waveguides.

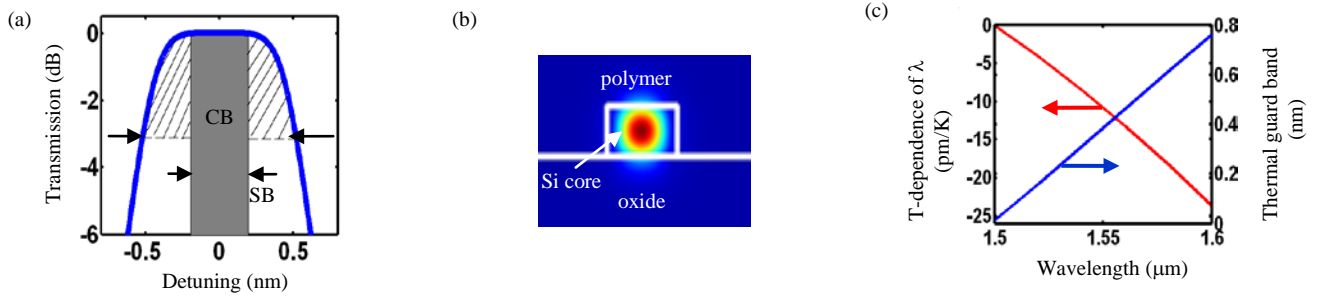


Fig. 28. (a) Illustration of extra channel bandwidth as thermal guard band (hatched region); CB: filter channel bandwidth; SB: signal information bandwidth; (b) cross section of the waveguide structure on an SOI substrate with a polymer cladding; (c) the left axis shows the wavelength temperature dependence of the filter, and the right axis shows the thermal guard band for 100 Gb/s wavelength channels.

Following the efficient broadband coupling engineering, we proceed to the second aspect of the design for temperature insensitive operation. Fig. 28(a) shows the concept of thermal guard band. The solid curve shows the optical filter passband response, and the solid filled rectangle shows the input optical signal information bandwidth, which can be as large as the 3-dB bandwidth of the filter channel [30], [33]. The remaining spectral portion shown by the hatched region illustrates the available thermal guard band. Our design for the temperature insensitive filter centers the complete athermal operating point at the wavelength channel with the smallest bandwidth (in our case this is at $\lambda = 1.5 \mu\text{m}$). This ensures that throughout the entire working wavelength range, the overall available thermal guard band is

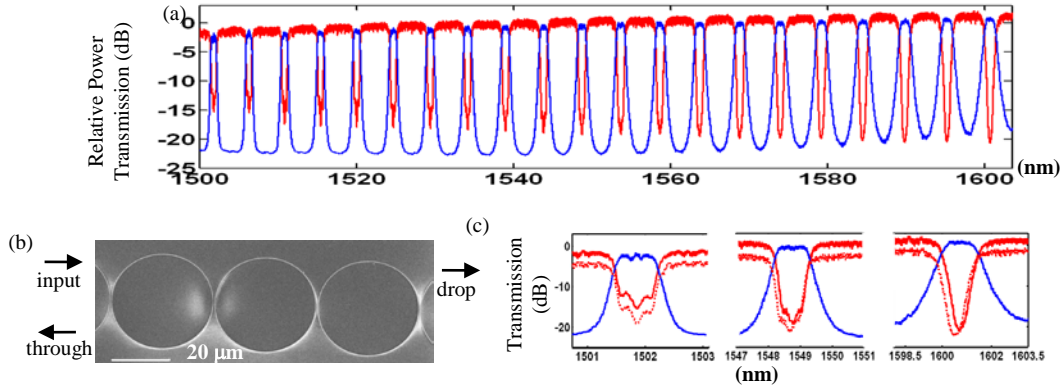


Fig. 29. (a) Measured transmission responses for the fabricated filter; (b) scanning-electron micrograph of the fabricated filter; (c) detailed measured spectra of three representative channels. The dotted lines show the through port responses after 10°C temperature rise.

optimally utilized. To achieve this, we overlay the silicon device with an acrylate polymer (see Fig. 28(b)) with a refractive index close to the oxide ($n=1.45$) and a large negative thermal-optic coefficient of $-4.5 \times 10^{-4}/\text{K}$ [28]. To increase the overlap between the optical field and the polymer cladding, the silicon device layer is thinned down to 144 nm, and the required waveguide width is calculated to be 425 nm for complete athermal operation at $\lambda=1.5 \mu\text{m}$. Fig. 28(c) shows the simulated temperature dependence of the filter over the entire working wavelength range, which increases from 0 pm/K at $\lambda=1.5 \mu\text{m}$ to 23 pm/K at $\lambda=1.6 \mu\text{m}$. To illustrate the operation of our filter, we consider the following scenario: if the filter is used for wavelength channels modulated at 100 Gb/s data rate, at $\lambda=1.5 \mu\text{m}$ the available guard bandwidth is small (3dB bandwidth 0.75 nm) but due to the centering of athermal operation to this wavelength, the filter channel shifts very little with the temperature. At the other end of the filter operation at $\lambda=1.6 \mu\text{m}$ the filter channel has a relatively large temperature dependence of -23 pm/K, but it also has a large available guard band of 0.75 nm (3 dB bandwidth 1.5 nm), thus allowing for $\pm 15^\circ \text{C}$ temperature fluctuations (see Fig. 28(c)). For lower data rate signals, even larger temperature fluctuations can be tolerated.

Device Fabrication and Experimental Results

The device is fabricated on an SOI wafer with a 144 nm thick silicon layer on top of a 3 μm thick buried oxide substrate. The devices are patterned using a JBX-9300FS electron beam lithography system, followed by plasma etching and spin coating the polymer cladding on the top surface. Details of fabrication and characterization are referred to [34] and [28].

Fig. 29(b) shows the scanning-electron micrograph of the fabricated device, and Fig. 29(a)

shows its measured transmission. 21 filter channels with more than 10 dB through-port extinction and 20 dB drop-port out-of-band rejection are obtained. The insertion loss of the filter can be estimated by the difference between the maxima of the through and drop ports to be less than 1 dB. In Fig. 29(c) we show three representative filter channels at wavelengths 1.5 μm , 1.55 μm and 1.6 μm , respectively. In comparison with the simulation results shown in Fig. 27(c), the 3-dB bandwidths agree well with the design, being 0.75 nm, 1.12nm and 1.5 nm for the corresponding channels. The out-of-band rejections in the drop port at lower wavelengths are limited to 22 dB, which are predicted to be higher in Fig. 27(c) (>25 dB). This deviation is believed to arise from the limited dynamic range of our measurement setup which has a relatively large noise floor. The reduction of the out-of-band rejections at longer wavelengths, as seen for the filter channels near $\lambda=1.6 \mu\text{m}$, is expected and in agreement with the theory. The through port responses are a little degraded from the design, as the extinction drops to 10 dB at $\lambda=1.5 \mu\text{m}$ instead of 15 dB, and the shape is also deformed. This is because the through port responses are very sensitive to the resonance frequency mismatches between the coupled resonators [35], which can be easily caused due to the imperfect fabrication processes.

The temperature behavior of the filter is also tested by heating the device using a thermal stage and measuring the transmission [28]. In Fig. 29(c) the corresponding through port responses after 10°C temperature rise are shown in dotted lines (deliberately moved down 3 dB for better illustration). We can verify that the filter is indeed athermal at $\lambda=1.5 \mu\text{m}$, and has wavelength temperature dependences of -12 pm/K and -25 pm/K at wavelengths 1.55 μm and 1.6 μm , respectively. This is a significant improvement compared to conventional unclad filters ($\sim 70 \text{ pm/K}$) [32].

In conclusion, we have demonstrated a temperature-insensitive wideband filter for on-chip Tb/s interconnects. In future, we envision addition of active switching functionality to the filter through carrier injection (either all-optically or electrically) and a high-performance switch with a switching speed on the order of nanoseconds is expected [32]. Such a wideband, temperature-insensitive optical switch would be a critical building-block component in future on-chip optical networks.

II.D Sub-wavelength Coherent Imaging of Silicon Microdisk Cavities using a Novel Dispersive Near-field Probing Technique

High quality factor and small mode volume of microdisk cavities have made them very attractive for a wide variety of applications including sensing, nonlinear optics, low threshold lasing, and cavity quantum electrodynamics. In most of these applications where the interaction of the optical modes of the micro resonator and an external perturbation at the proximity of the resonator is required, knowing the near field profile of the cavity mode is essential. For this purpose, we have developed a technique for sub-wavelength near-field imaging of the optical modes in microdisk cavities by measuring the effect of a small perturbation (caused by the scanning AFM tip) on the transmission amplitude and phase of the coupled waveguide microdisk cavity. Different effect of the perturbation caused by the AFM tip on the optical modes in the cavity (i.e. loss, resonance shift, mode coupling) and their effect in the transmission amplitude and phase of the system are studied. The experimental results confirm that the primary factor that

contributes to the change in the transmission amplitude and phase is the shift in the resonance wavelength of the cavity caused by the perturbation.

Conventional Near-field scanning optical microscopy (NSOM) techniques are based on the coupling of light from the evanescent field of the optical modes to the collecting fiber, through the NSOM sub-wavelength aperture probe. The spatial resolution of this technique is limited by the relatively large size of the aperture which is required to couple sufficient power to the NSOM probe. Furthermore, in the case of high Q cavities, the large NSOM probe significantly perturbs the optical modes of the cavity and makes it impossible to measure the actual mode profile of the resonant mode of the cavity. As an alternative technique, the aperture-less NSOM technique has been proposed that is based on the far-field collection of the light scattered from a sub-wavelength perturbation in the near-field region of the desired mode [8]. Aperture-less NSOM technique has also been used to characterize the mode profile of the guided mode in an optical waveguide by measuring the transmission loss of the waveguide instead of the scattered light power [9]. In this work, we present an alternative technique for the characterization of the mode profile of high Q cavities based on the effect of small perturbations on the transmission amplitude and phase of a coupled waveguide-cavity system. The small perturbation in this case is a small AFM tip that scans the surface of the cavity and is modeled by a small dielectric perturbation on the surface of the cavity. The schematic of this is shown in figure 30. The perturbation of the cavity mode caused by the tip affects the cavity in three different ways namely; 1) Increasing the microdisk cavity loss due to the scattering and absorption through the perturbation. 2) Shifting the resonance wavelength of the cavity due to the small refractive index change, 3) Coupling the degenerate clockwise and counterclockwise modes inside the microdisk cavity that leads to mode splitting [10]. Although all of these factors affect the coupled waveguide-cavity transmission amplitude and phase at the same time, and their effects scale with the cavity mode field intensity at the perturbation position, nevertheless, their effects are completely different and depend on the cavity quality factor, the waveguide-cavity coupling and the detuning of the input laser wavelength from the resonance wavelength of the unperturbed cavity.

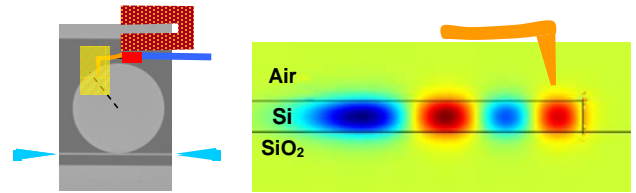


Figure 30 (left) Schematic of the experimental set up. Light is coupled into and out of the structure through two tapered fibers. A scanning AFM tip is used as a controllable perturbation. (right) The cross section of the electric field profile of a fourth order radial mode in a microdisk cavity simulated using finite element method.

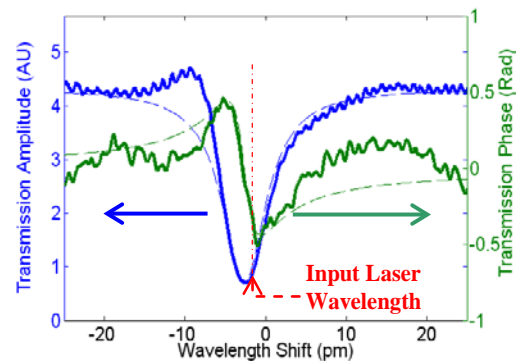


Figure 31, Solid (dashed) lines show measured (simulated) transmission amplitude (right) and phase (left) of the coupled waveguide and microdisk cavity without AFM tip perturbation.

To experimentally investigate the effect of a small perturbation on the optical modes in a micro-resonator, a microdisk cavity with a diameter of $40\mu\text{m}$ is fabricated on an SOI substrate. The thickness of the silicon slab layer is 230 nm . The light is coupled to the microdisk cavity through a waveguide and coupling between the waveguide and microdisk cavity is adjusted to obtain close to critical coupling [11]. Figure 31 shows the transmission of the microdisk cavity for TE polarization (Main components of E field is in the plane of the resonator) in a small wavelength range around the microdisk resonance mode at $\lambda=1529.71\text{ nm}$. The resonant mode of the unperturbed cavity has a loaded Q (i.e., Q after coupling to the waveguide) of $233,000$ that correspond to a resonance line width of 6.56 pm . The phase response of the cavity is also shown in Fig 6 and is obtained by heterodyne detection of the output signal. Taking the amplitude and phase information together, we estimate that under-coupled case where the coupling Q (i.e., $Q_c=796,000$) is larger than the intrinsic Q (i.e., $Q_i=329,000$) of the cavity. The cavity mode is perturbed by a small AFM tip with a diameter of 20 nm and a tapering angle of 20 degree. The input laser is initially 0.85 pm red shifted in respect to the microdisk cavity resonant mode.

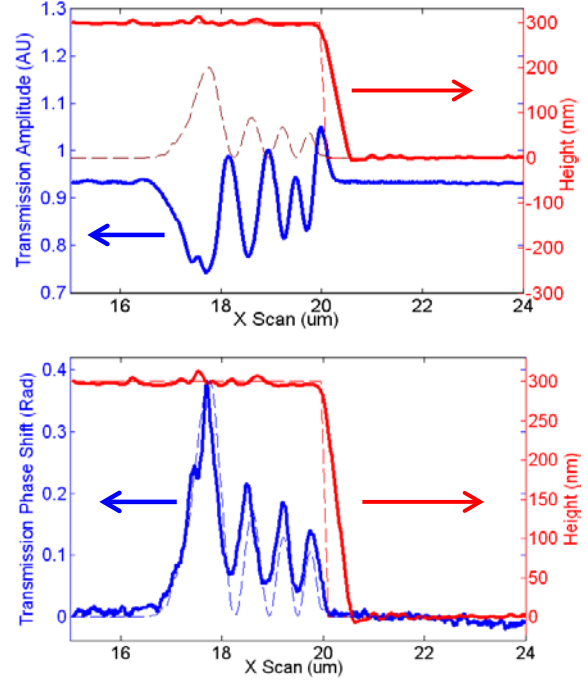


Figure 32, Solid blue lines (left) show the transmission amplitude (top) and phase (down) of the coupled waveguide and microdisk cavity as AFM tips scan the microdisk cavity in the radial direction. Dashed blue lines (left) show the radial pattern of the normalized electrical field intensity. The solid (dashed) red curves (right) show the actual (ideal) AFM topography scan.

Figure 32 shows the change in the transmission phase and amplitude as the AFM scans the surface of the microdisk cavity in radial direction. The interaction between the AFM tip and the optical mode in the microdisk cavity depends on the electrical field intensity at the tip position. As it can be observed from Figure 32 the resonant mode is a fourth-order radial mode. The effect of AFM tip perturbation on the coupled waveguide-cavity device is mainly causing a positive phase shift and a reduction in the transmission amplitude. Considering the fact that the input laser is red shifted with respect to the unperturbed resonant mode of the cavity (refer to Figure 31), these changes in the transmission amplitude and phase are mainly contributed by a red shift in the resonant mode of the cavity caused by the AFM tip perturbation. If the loss due to scattering and absorption was the major effect it should have resulted to an increase in the transmission amplitude and a reduction in the transmission phase (caused by the reduction in the intrinsic Q of the cavity). The amount of the shift in the cavity resonant is proportional to the

electrical field intensity at the tip position. The maximum shift appears when the tip is at the position corresponding to the maximum field intensity of the main resonant mode lobe. The amount of the wavelength shift can be calculated from both amplitude and phase responses and in both cases result in very similar shifts of about 1.25 pm. The proposed technique provides a powerful tool for the investigation of optical modes of microdisk resonators with sub-wavelength ($\sim 20\text{nm}$) spatial resolution. Moreover, the proposed technique could be a useful tool for studying near-field interaction with a perturbative particle in the proximity of the resonator.

II.E Small disk Si microresonators

In many Si photonics applications where features such as compactness, smaller mode volume, larger FSR, and single resonance mode condition over the FSR range are required, the resonator dimensions need to be shrunk. This is especially important for the large-scale dense photonic integration of many resonator-based functionalities and devices. A major problem with microring and racetrack resonators is that at very small bending radii, the inner sidewall of the resonator forces the mode energy distribution out of the resonator, resulting in more energy leakage and the presence of fabrication imperfections at two sidewalls of the microring and racetrack degrades the Q . In contrast to a microring or a racetrack, a microdisk resonator has only one sidewall and therefore the Q suffers less from fabrication imperfections.



Figure 33 The cross sections of the simulated electric energy distributions of (a) the 1st and (b) the 2nd radial order mode of a silicon microdisk resonator with a radius of $1.4\mu\text{m}$ and a thickness of 200 nm. The resonance wavelengths of the modes are around 1550 nm, and the corresponding azimuth mode numbers are 11 and 8 for the 1st mode and the 2nd mode, respectively. The polarization considered is TE (electric field is predominantly in the plane of the disk).

During this period of the PECASE, we investigated in detail the ultimate size miniaturization of Si microdisk resonators as well as their potential as building block elements for dense integrated photonics.

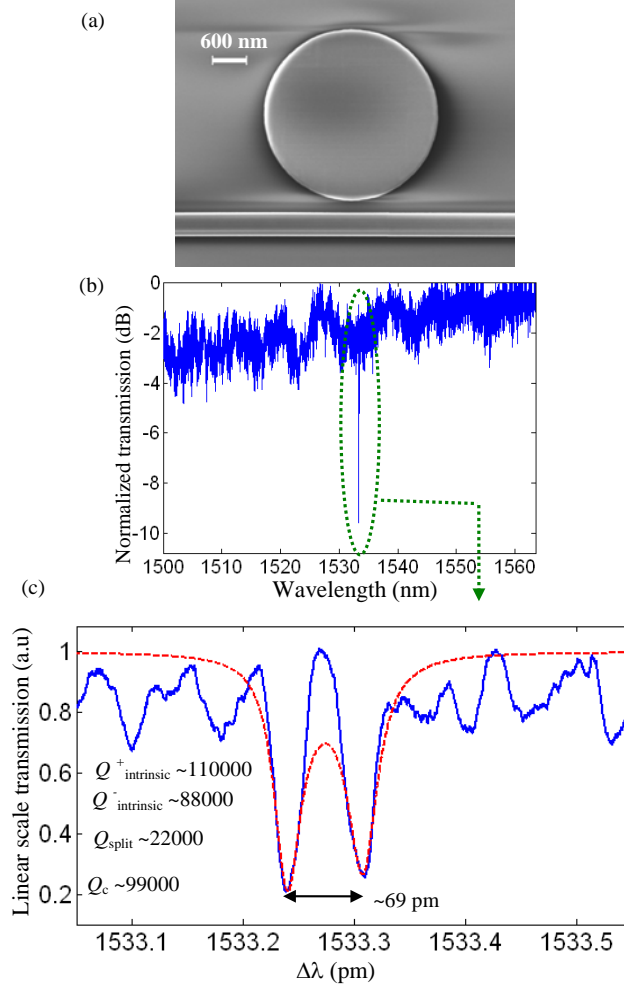


Figure 34 (a) SEM image of a microdisk resonator with a radius of $1.53\mu\text{m}$ coupled to a waveguide with a width of 400 nm . The gap between the waveguide and the resonator is $\sim 210\text{ nm}$. The thickness of the Si microdisk is 230 nm and there is a thin HSQ layer with a thickness of $\sim 60\text{ nm}$ on top of the microdisk and the waveguide. (b) Transmission spectrum of the resonator showing the 1st radial order TE mode. (c) Detailed resonance spectrum of the 1st radial mode of this resonator, which shows resonance splitting. By fitting theory to experiment, the intrinsic Q s $\approx 110,000$ and $88,000$ were obtained for the two standing-wave modes. The value of the coupling $Q \sim 99,000$ in the fitted data is close to the calculated value from coupled-mode theory. The azimuth harmonic mode of this mode is $m=12$ and its mode volume is $\sim 0.15 (\lambda_0)^3 = 6.3 (\lambda_0/n)^3$ with $n = 3.475$.

The first thing we noticed through simulations was that by adjusting the radius and the thickness of the microdisk, the higher-order radial modes are strongly suppressed because of their radiative leakage, thereby resulting in a pure single-mode operation for a very wide wavelength range. As an example, figures 33(a) and 33 (b) show the cross sections of the electric energy of the 1st and the 2nd radial order modes with a TE polarization (electric field is predominantly in the plane of the disk) for a microdisk resonator with a radius of $1.4\mu\text{m}$ and a thickness of 200nm . As shown in this figure, the 1st order mode is a confined mode, while the 2nd order mode is strongly radiative. We fabricated small microdisk resonators with radii ranging from 1.5 to $2\mu\text{m}$ to experimentally study their performance. We considered a range of Si device layer thicknesses from 210 to 235 nm . Figure 34(a) shows the SEM image of a microdisk resonator with a radius of $1.53\mu\text{m}$ coupled to a straight ridge waveguide with a width of 400 nm . Also, figure 34(b)

shows the transmission spectrum of this resonator for which one resonance mode with a pretty strong extinction is seen over the entire FSR range. This resonance mode is the 1st radial order TE mode, and the theoretical simulations accurately predict the azimuth mode number $m=12$. From the simulations, the FSR and the mode volume of this mode are $\text{FSR} \approx 70 \text{ nm}$ and $6.3 (\lambda/n)^3$ (with $n = 3.475$), respectively. Figure 34(c) shows a zoomed view of the resonance mode spectrum showing the resonance splitting as a result of coupling between the CW and CCW modes and the occurrence of two standing-wave modes. By fitting the experimental data to theoretical simulations, the device parameters were extracted (see inset of Figure 34(c)). From the fitting results, the intrinsic Q s $\sim 110,000$ and $88,000$ for the two standing-wave modes of the resonator were obtained. These are the highest Q s reported for such a small Si microdisk resonator (with a radius of $1.53 \mu\text{m}$) on a SiO_2 substrate in a SOI platform. We believe that by further optimizing the fabrication process, the Q can be improved by at least a factor of two.

The feasibility of such an ultra-compact high Q resonator as a building block component for dense integration was investigated by designing and fabricating a series of single and coupled-resonator add-drop filters. The coupling coefficients in the filters were obtained from the temporal coupled-mode theory. The resonance frequency and mode profiles of the resonator was calculated and incorporated into the coupling integral equation to find the required optimal gaps between the resonators for the required coupling coefficients. Figure 35(a) shows the drop port spectrum of a single-resonator add-drop filter with an $\text{FSR} \approx 57 \text{ nm}$. The inset shows the SEM image of the filter made of an oxide-clad microdisk with $r = 2 \mu\text{m}$ and thickness 230 nm . A linewidth of 50 pm was measured for this filter. Figure 35(b) shows the drop port spectrum of a 2nd order filter made of two resonators with the same dimensions as the one in figure 35(a). As can be seen from both figure 35(a) and (b), all the higher order modes are in the noise floor. Figure 35(c) shows the detailed spectrum of the drop and through ports of the filter shown in figure 35(b). A 3-dB bandwidth of 0.4 nm was obtained for this filter and more than 10 dB extinction was obtained for the through port. From theory, the expected extinction is more than 60 dB. However, the resonance misalignment of the individual resonators and changes in the gaps introduced by fabrication imperfection have limited the through port extinction.

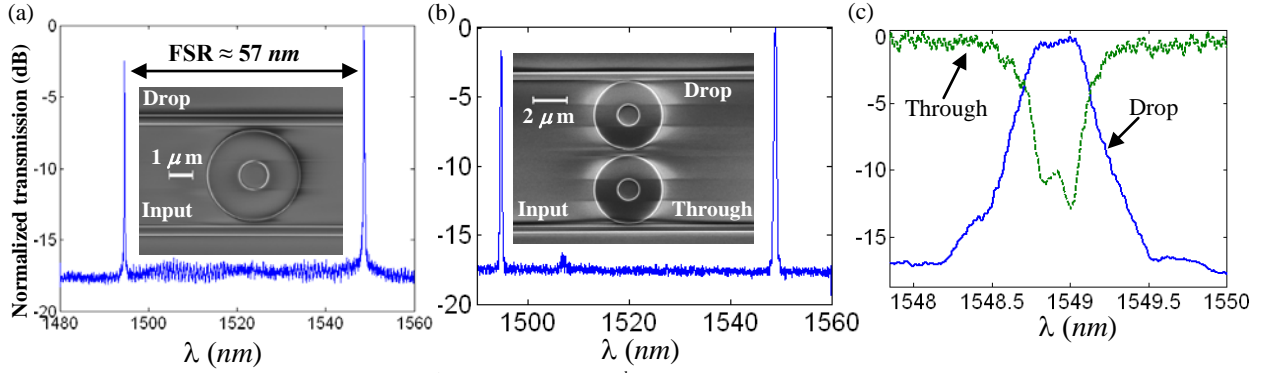


Figure 35. The drop port spectrum of (a) 1st order and (b) a 2nd order filter with an $\text{FSR} \approx 57 \text{ nm}$. The insets in (a) and (b) show the SEM images of the fabricated filters. The waveguide width and thickness are 400 nm and 230 nm respectively. The employed microdisk resonator has $r=2 \mu\text{m}$ with an inner hole with $r=0.6 \mu\text{m}$ perforated at its center. In (a), the gap between the waveguide and the resonator is 240 nm . In (b), the gap between the waveguide and resonator is 100 nm and between the resonators is 350 nm . (c) Detailed spectra of drop and through ports of the filter in (b).

As a further step in this feasibility study for large-scale photonic integration, we designed and fabricated ultra-compact optical filter banks made of add-drop filters. This is shown in figure 36 (a) where there is one input bus waveguide for all the resonators, and each resonator has its own drop port. The sizes of the resonators are adjusted to have different resonant wavelengths. In this filter bank there are six Si microdonut resonators with a thickness of 230 nm and external radii varying from $1.92 \mu\text{m}$ to $1.97 \mu\text{m}$, with a radial step change of 10 nm . From the theoretical simulations, a 10 nm change in the radius of these resonators results in a $\sim 6 \text{ nm}$ shift in the resonance wavelength. Figure 36(b) shows the SEM image of one of the add-drop structures in the filter bank and figure 36(c) shows the transmission spectrum of the drop ports of the filter bank. As can be seen, all the channels are almost equally spaced in the spectrum. For these channels, linewidths in the range 50 pm to 100 pm were obtained. The key advantages of such a filter bank architecture using such small high-Q microdisk resonators are as follows: (i) The individual resonators in the filter are high Q. As a result, each filter in the filter bank can be low loss with very narrow linewidths. (e.g. for a $Q_0=100,000$ and $Q_c = 10,000$, the filter has a loss $\sim 0.4 \text{ dB}$ and a linewidth of 0.3 nm at 1550 nm). (ii) More filter channels could be accommodated within the large FSR and (iii) External and internal radii of the microdonut resonators in the filter bank can be utilized to tune the wavelength resonances. In the future, we anticipate the small radii microdisk resonators to become universal building blocks for VLSI dense photonic integrated circuits in SOI.

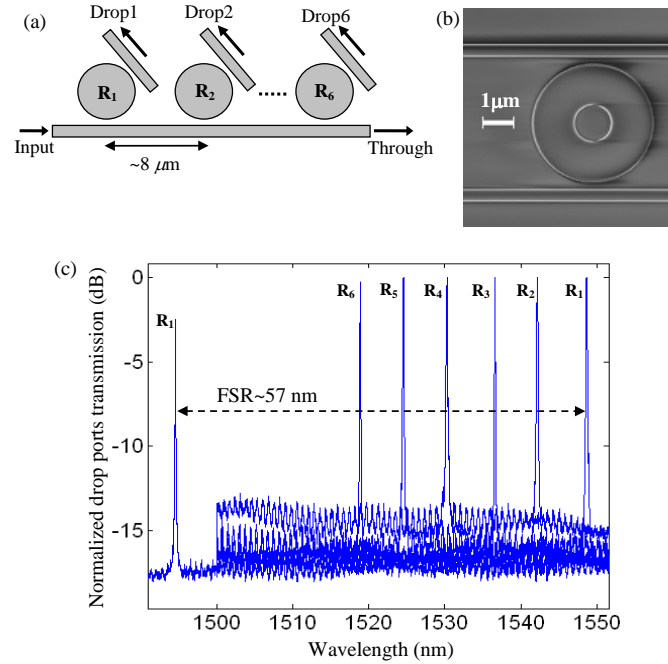


Figure 36 (a) An array of add-drop resonator filters suitable for in-plane spectral analysis and signal processing. The radius of the resonators varies from $1.92\ \mu\text{m}$ to $1.97\ \mu\text{m}$ with a radial step change of 10 nm. (b) The SEM image of one of the fabricated resonators in the array, which has a radius of $1.97\ \mu\text{m}$. The structure is covered with an oxide cladding. (c) Measured transmission of the drop ports of the array shown in (a). The FSR is $\sim 57\ \text{nm}$ and the spectral linewidth was designed to be in the range of 50 to 100 pm.

References

- [1] E. Shah Hosseini, S. Yegnanarayanan, A.H. Atabaki, M. Soltani, and A. Adibi, "High Quality Planar Silicon Nitride Microdisk Resonators for Integrated Photonics in the Visible Wavelength Range," *Optics Express*, **17**, 14543 (2009).
- [2] M. Chin and S. Ho, "Design and Modeling of Waveguide-Coupled Single-Mode Microring Resonators," *J. Lightwave Technol.* **16**, 1433–1446 (1998).
- [3] J. Hu, N. Carlie, N. Feng, L. Petit, A. Agarwal, K. Richardson, and L. Kimerling, "Planar waveguide-coupled, high-index-contrast, high-Q resonators in chalcogenide glass for sensing," *Opt. Lett.* **33**, 2500–2502 (2008).
- [4] B. Momeni, S. Yegnanarayanan, M. Soltani, A. A. Eftekhari, E. S. Hosseini, and A. Adibi, "Silicon nanophotonic devices for integrated sensing," *J. Nanophoton.* **3**(1), 031001 (2009).
- [5] R. F. Wolffenbuttel, "State-of-the-art in integrated optical microspectrometers," *IEEE Trans. Instrum. Meas.* **53**(1), 197–202 (2004).
- [6] D. S. Goldman, P. L. White, and N. C. Anheier, "Miniaturized spectrometer employing planar waveguides and grating couplers for chemical analysis," *Appl. Opt.* **29**(31), 4583–4589 (1990).
- [7] D. Sander, M.-O. Dückler, O. Blume, and J. Müller, "An optical microspectrometer in SiON-slab-waveguides," *Proc. SPIE* **2686**, 100–107 (1996).
- [8] Y. Maruyama, K. Sawada, H. Takao, and M. Ishida, "A novel filterless fluorescence detection sensor for DNA analysis," *IEEE Trans. Electron. Dev.* **53**(3), 553–558 (2006).
- [9] D. A. Zauner, A. M. Jorgensen, T. A. Anhoj, and J. Hübner, "Concave reflective SU-8 photoresist gratings for flat-field integrated spectrometers," *Appl. Opt.* **45**(23), 5877–5880 (2006).
- [10] Y. Komai, H. Nagano, K. Okamoto, and K. Kodate, "Compact spectroscopic sensor using a visible arrayed waveguide grating," *Jpn. J. Appl. Phys.* **45**(No. 8B), 6742–6749 (2006).
- [11] S. Janz, A. Balakrishnan, S. Charbonneau, P. Cheben, M. Cloutier, A. Delâge, K. Dossou, L. Erickson, M. Gao, P. A. Krug, B. Lamontagne, M. Packirisamy, M. Pearson, and D.-X. Xu, "Planar waveguide Echelle gratings in silica-on-silicon," *IEEE Photon. Technol. Lett.* **16**(2), 503–505 (2004).
- [12] Y. Hibino, "Recent advances in high-density and large-scale AWG multi/demultiplexers with higher index contrast silica-based PLCs," *IEEE J. Sel. Top. Quantum Electron.* **8**(6), 1090–1101 (2002).
- [13] H. Kosaka, T. Kawashima, A. Tomita, M. Notomi, T. Tamamura, T. Sato, and S. Kawakami, "Superprism phenomena in photonic crystals: toward microscale lightwave circuits," *J. Lightwave Technol.* **17**(11), 2032–2038 (1999).
- [14] B. Momeni, J. Huang, M. Soltani, M. Askari, S. Mohammadi, M. Rakhshandehroo, and A. Adibi, "Compact wavelength demultiplexing using focusing negative index photonic crystal superprisms," *Opt. Express* **14**(6), 2413–2422 (2006).
- [15] B. Momeni, M. Chamanzar, E. S. Hosseini, M. Askari, M. Soltani, and A. Adibi, "Strong angular dispersion using higher bands of planar silicon photonic crystals," *Opt. Express* **16**(18), 14213–14220 (2008).
- [16] B. Momeni, and A. Adibi, "An approximate effective index model for efficient analysis and control of beam propagation effects in photonic crystals," *J. Lightwave Technol.* **23**(3), 1522–1532 (2005).

- [17] B. Momeni, and A. Adibi, "Preconditioned superprism-based photonic crystal demultiplexers: analysis and design," *Appl. Opt.* **45**(33), 8466–8476 (2006).
- [18] E. Shah Hosseini, S. Yegnanarayanan, A. H. Atabaki, M. Soltani, and A. Adibi, "High quality planar silicon nitride microdisk resonators for integrated photonics in the visible wavelength range," *Opt. Express* **17**(17), 14543–14551 (2009).
- [19] J. J. Baumberg, N. M. B. Perney, M. C. Netti, M. D. C. Charlton, M. Zoorob, and G. J. Parker, "Visible wavelength super-refraction in photonic crystal superprisms," *Appl. Phys. Lett.* **85**(3), 354–356 (2004).
- [20] B. Momeni, Q. Li, and A. Adibi, "Ultra-compact implementation of planar superprism-based demultiplexers in silicon," *in preparation*.
- [21] T. Baba, and D. Ohsaki, "Interfaces of photonic crystals for high efficiency light transmission," *Jpn. J. Appl. Phys.* **40**(Part 1, No. 10), 5920–5924 (2001).
- [22] B. Momeni, and A. Adibi, "Adiabatic matching stage for coupling of light to extended Bloch modes of photonic crystals," *Appl. Phys. Lett.* **87**(17), 171104 (2005).
- [23] K. Okamoto, *Fundamentals of Optical Waveguides*, San Diego: Academic Press, 2000.
- [24] P. E. Barclay, K. Srinivasan, O. Painter, T. J. Watson, B. Lev, and H. Mabuchi, "Integration of fiber-coupled high-Q SiN_x microdisks with atom chips," *Appl. Phys. Lett.* **89**(13), 131108 (2006).
- [25] B. Momeni, M. Askari, E. S. Hosseini, A. Atabaki, and A. Adibi, "An on-chip silicon grating spectrometer using a photonic crystal reflector," *submitted for publication*.
- [26] M. Notomi, "Theory of light propagation in strongly modulated photonic crystals: Refractionlike behavior in the vicinity of the photonic band gap," *Phys. Rev. B* **62**(16), 10696–10705 (2000).
- [27] J. Teng, P. Dumon, W. Bogaerts, H. Zhang, X. Jian, X. Han, M. Zhao, G. Morthier, and R. Baets, "Athermal silicon-on-insulator ring resonators by overlaying a polymer cladding on narrowed waveguides," *Opt. Express* **17**, 14627–14633 (2009).
- [28] P. Alipour, E. Shah Hosseini, A. A. Eftekhari, B. Momeni, and A. Adibi, "Athermal performance in high-Q polymer-clad silicon microdisk resonators," *Opt. Lett.* **35**, 3462–3464 (2010).
- [29] G. Gulsen and M. Naci Inci, "Thermal optical properties of TiO₂ films," *Opt. Mater.* **18**, 373–381, (2002).
- [30] K. Bergman, "Silicon photonic on-chip optical interconnection networks," in *Frontiers in Nanophotonics and Plasmonics*, Guarujá, Brazil, Nov 2007.
- [31] A. Shacham, K. Bergman, and L. P. Carloni, "Photonic networks-on-chip for future generations of chip multiprocessors," *IEEE Trans. Comput.*, vol. 57, no. 9, pp. 1246–1260, Sep. 2008.
- [32] Y. Vlasov, W. M. J. Green, and F. Xia, "High-throughput silicon nanophotonic wavelength-insensitive switch for on-chip optical networks," *Nature Photon.*, vol. 2, pp. 242–246, Apr. 2008.
- [33] B. G. Lee, A. Biberman, P. Dong, M. Lipson, and K. Bergman, "All-Optical comb switch for multiwavelength message routing in silicon photonic networks," *IEEE Photon. Technol. Lett.*, vol. 20, no. 10, pp. 767–769, May 2008.
- [34] Q. Li, M. Soltani, S. Yegnanarayanan, and A. Adibi, "Design and demonstration of compact, wide bandwidth coupled-resonator filters on a silicon-on-insulator platform," *Opt. Express*, vol. 17, no. 4, pp. 2247–2254, Feb. 2009.
- [35] Q. Li, M. Soltani, A. H. Atabaki, S. Yegnanarayanan, and A. Adibi, "Quantitative modeling of coupling-induced resonance frequency shift in microring resonators," *Opt. Express*, vol. 17, no. 26, pp. 23474–23487, Dec. 2009.

III. Publications and Presentations

III.A Journal papers

1. B. Momeni, E. Shah Hosseini, and A. Adibi, "Planar photonic crystal microspectrometers in silicon-nitride for the visible range," *Optics Express*, **17**, 17060 (2009).
2. Q. Li, M. Soltani, S. Yegnanarayanan, and A. Adibi, "Design and demonstration of compact, wide bandwidth coupled-resonator filters on a silicon-on-insulator platform," *Optics Express*, **17**, 2247 (2009).
3. B. Momeni, E. Shah Hosseini, M. Askari, M. Soltani, and A. Adibi, "Integrated photonic crystal spectrometers for sensing applications," *Optics Communications*, **282**, 3168 (2009).
4. B. Momeni, S. Yegnanarayanan, M. Soltani, A. Eftekhari, E. Shah Hosseini, and A. Adibi, "Silicon nanophotonic devices for integrated sensing," *Invited Paper, Journal of Nanophotonics*, **3**, 031001 (2009).
5. M. Soltani, S. Yegnanarayanan, A. Adibi, "Ultra-high Q planar silicon microdisk resonators for chip-scale silicon photonics" *Optics Express* **15**, 4694(2007).
6. M. Soltani, Q. Li, S. Yegnanarayanan, and A. Adibi, "Improvement of thermal properties of ultra-high Q silicon microdisk resonators," *Optics Express*, **15**, 17305 (2007).
7. B. Momeni, S. Yegnanarayanan, M. Soltani, A. Eftekhari, E. Shah Hosseini, and A. Adibi, "Silicon nanophotonic devices for integrated sensing," **Invited Paper**, *Journal of Nanophotonics*, **3**, 031001 (2009).
8. S. Yegnanarayanan, M. Soltani, E. Shah Hosseini, A. Eftekhari, and A. Adibi, "Microresonators in CMOS compatible substrates," **Invited Paper**, *Journal of Nanoscience and Nanotechnology*, Special Issue on Nanooptics and Nanophotonics (accepted, To appear November 2009).
9. E. Shah Hosseini, S. Yegnanarayanan, A. Atabaki, M. Soltani, and A. Adibi, "Systematic design and fabrication of high- Q pulley-coupled planar silicon nitride microdisk resonators," *Opt. Express* **18**(3), 2010.
10. A.H. Atabaki, B. Momeni, A. A. Eftekhari, E. Shah Hosseini, S. Yegnanarayanan, and A. Adibi, "Tuning of Resonance-Spacing in a Traveling-Wave Resonator Device," *Opt. Express* **18**(9), 2010.
11. M. Soltani, S. Yegnanarayanan, Q. Li, and A. Adibi, "Systematic Engineering of Waveguide-Resonator Coupling for Silicon Microring/Microdisk/Racetrack Resonators: Theory and Experiment," *IEEE Journal of Quantum Electron.*, **46**(8), 2010.
12. Q. Li, M. Soltani, A. Atabaki, S. Yegnanarayanan, and A. Adibi, "Quantitative modeling of coupling induced resonance frequency shift in microring resonators," *Opt. Express* **17**(26), 2009.
13. M. Soltani, Q. Li, S. Yegnanarayanan, and A. Adibi, "Ultimate Miniaturization and Scaling Limits for Silicon Microdisk Resonators: Impact on Q and Thermal Properties," "Toward ultimate miniaturization of high Q silicon traveling-wave microresonators," *Opt. Express* **18**, 2010.
14. Q. Li, S. Yegnanarayanan, M. Soltani, P. Alipour, and A. Adibi, "A Temperature-Insensitive Third-Order Coupled-Resonator Filter for On-Chip Terabit/s Optical Interconnects," *IEEE Photon. Tech. Lett.* **22**, 1768, 2010

III.B Conference presentations

1. Q. Li, S. Yegnanarayanan, A. A. Eftekhari, and A. Adibi, "Low-loss microdisk-based delay lines for narrowband optical filters," *Integrated Photonics Research Silicon and Nanophotonics OSA Technical Digest (CD) (Optical Society of America)*, paper IMC7, July 2010, Monterey.
2. M. Soltani, S. Yegnanarayanan, Q. Li, A. H. Atabaki, A. A. Eftekhari and A. Adibi, "Sustained GHz Oscillations in Ultra-high Q Silicon Microresonators," *IEEE Lasers and Electro-Optics Society, (LEOS), 22nd Annual Meeting, Belek-Antalya, Turkey, 4-8 October 2009.*
3. M. Soltani, Q. Li, S. Yegnanarayanan, B. Momeni, A. A. Eftekhari and A. Adibi, "Large-scale Array of Small High- Q Microdisk Resonators for On-chip Spectral Analysis," *IEEE Lasers and Electro-Optics Society, (LEOS), 22nd Annual Meeting, Belek-Antalya, Turkey, 4-8 October 2009.*

4. A. H. Atabaki, A. A. Eftekhari, S. Yegnanarayanan, and A. Adibi, "Sub-Microsecond Thermal Reconfiguration of Silicon Photonic Devices," IEEE Lasers and Electro-Optics Society, (LEOS), 22nd Annual Meeting, Belek-Antalya, Turkey, 4-8 October 2009.
5. A.H. Atabaki, A. A. Eftekhari, S. Yegnanarayanan, and A. Adibi, "Enhancing Thermal Reconfiguration Speed for Silicon Photonics Applications," Integrated Photonics and Nanophotonics Research and Applications, IPRNA 2009, (Optical Society of America), Honolulu, Hawaii, 12 July 2009.
6. M. Soltani, Q. Li, S. Yegnanarayanan, and A. Adibi, "Implementation of Single and Coupled Resonator Filters Using Ultimate Miniaturized Silicon Microdisk Resonators," Integrated Photonics and Nanophotonics Research and Applications, IPRNA 2009, (Optical Society of America), Honolulu, Hawaii, 12 July 2009.
7. M. Soltani, S. Yegnanarayanan, Q. Li, and A. Adibi, "Systematic Engineering of Waveguide-Resonator Coupling for Silicon Microring/Microdisk Resonators," Integrated Photonics and Nanophotonics Research and Applications, IPRNA 2009, (Optical Society of America), Honolulu, Hawaii, 12 July 2009.
8. P. Alipour, A. H. Atabaki, A. A. Eftekhari, and A. Adibi, "Athermal Performance in Titania-Clad Microring Resonators on SOI," in *Integrated Photonics Research, Silicon and Nanophotonics*, OSA Technical Digest (CD) (Optical Society of America, 2010), paper IMC6.
9. S. Yegnanarayanan, M. Soltani, Q. Li, and A. Adibi, "Optimized Silicon Microdisk with High Sensitivity for Label-free Lab-on-a-Chip Sensing Applications," Conference on Lasers and Electro-Optics, CLEO/QELS 2009, Baltimore, Maryland, 31st May - 5th, June 2009.
10. A. H. Atabaki, S. Yegnanarayanan, and A. Adibi, "Resonance Spacing Tuning in Traveling-wave Resonators," Conference on Lasers and Electro-Optics, CLEO/QELS 2009, Baltimore, Maryland, 31st May - 5th, June 2009.
11. A. Eftekhari, M. Soltani, S. Yegnanarayanan, and A. Adibi, "Sub-Wavelength Imaging of Optical Modes in Silicon Microdisk Cavities using a Near-Field Probing Technique," Conference on Lasers and Electro-Optics, CLEO/QELS 2009, Baltimore, Maryland, 31st May - 5th, June 2009.
12. A. H. Atabaki, M. Soltani, A. A. Eftekhari, S. Yegnanarayanan, and A. Adibi, "Optimization of Metallic-microheaters for Reconfigurable Silicon Photonics," Conference on Lasers and Electro-Optics, CLEO/QELS 2009, Baltimore, Maryland, 31st May - 5th, June 2009.
13. M. Soltani, Q. Li, S. Yegnanarayanan, and A. Adibi, "Ultimate Miniaturization of Single and Coupled Resonator Filters in Silicon Photonics," Conference on Lasers and Electro-Optics, CLEO/QELS 2009, Baltimore, Maryland, 31st May - 5th, June 2009.
14. Q. Li, M. Soltani, S. Yegnanarayanan, and A. Adibi, "A Compact Wideband Flat-band Filter for Silicon Photonic Applications," Conference on Lasers and Electro-Optics, CLEO/QELS 2009, Baltimore, Maryland, 31st May - 5th, June 2009.
15. A. Adibi, B. Momeni, S. Yegnanarayanan, M. Soltani, and A. Eftekhari, "Lab-on-a-Chip Sensing using Ultra-Compact Si Nanophotonic Structures," Invited Paper, The IEEE Lasers and Electro-Optics Society (LEOS) Winter Topical Meeting Series on Nanophotonics, Innsbruck, Austria, 12-14 January 2009.
16. A. Eftekhari, M. Soltani, S. Yegnanarayanan, and A. Adibi, "Sub-Wavelength Imaging of Optical Modes in Silicon Microdisk Cavities using a Near-Field Probing Technique," The IEEE Lasers and Electro-Optics Society (LEOS) Winter Topical Meeting Series on Nanophotonics, Innsbruck, Austria, 12-14 January 2009.
17. E. Shah Hosseini, S. Yegnanarayanan, and A. Adibi, "Ultra-High Quality Factor Silicon Nitride Planar Microdisk Resonators for Integrated Photonics in the Visible Range: A New Coupling Scheme," The IEEE Lasers and Electro-Optics Society (LEOS) Winter Topical Meeting Series on Nanophotonics, Innsbruck, Austria, 12-14 January 2009.
18. A. H. Atabaki, Q. Li, S. Yegnanarayanan, M. Chamanzar, E. Shah Hosseini, A. A. Eftekhari, M. Soltani, B. Momeni, and A. Adibi, "Interferometrically-Coupled Traveling-Wave Resonators for

- Nonlinear Optics Applications ,” The IEEE Lasers and Electro-Optics Society (LEOS) Winter Topical Meeting Series on Nanophotonics, Innsbruck, Austria, 12-14 January 2009.
19. E. Shah Hosseini, S. Yegnanarayanan, and A. Adibi, “High quality factor microdisk resonators for chip-scale visible sensing,” IEEE Lasers and Electro-Optics Society, (LEOS), 21st Annual Meeting, Newport Beach, California, 9-13 November 2008.
 20. A. A. Eftekhar, M. Soltani, S. Yegnanarayanan, and A. Adibi, “Characterization of the effect of small perturbations on the optical modes in high Q microdisk cavities,” IEEE Lasers and Electro-Optics Society, (LEOS), 21st Annual Meeting, Newport Beach, California, 9-13 November 2008.
 21. A. H. Atabaki, S. Yegnanarayanan, B. Momeni, E. Shah Hosseini, Q. Li, M. Soltani, A. A. Eftekhar, and A. Adibi, “Implementation of a coupling-tunable resonator for efficient high-bandwidth nonlinear silicon photonics applications,” IEEE Lasers and Electro-Optics Society, (LEOS), 21st Annual Meeting, Newport Beach, California, 9-13 November 2008.
 22. A. H. Atabaki, M. Soltani, Q. Li, S. Yegnanarayanan, and A. Adibi, “Modeling of Thermal Properties of Silicon-on-Insulator Traveling-Wave Resonators,” *Frontiers in Optics*, OSA Technical Digest, (Optical Society of America), Rochester, New York, October 19, 2008.
 23. E. Shah Hosseini, S. Yegnanarayanan, M. Soltani, and A. Adibi, “Ultra-High Quality Factor Microdisk Resonators for Chip-Scale Visible Integrated Photonics,” *Frontiers in Optics*, OSA Technical Digest, (Optical Society of America), Rochester, New York, October 19, 2008.
 24. M. Soltani, Q. Li, S. Yegnanarayanan, and A. Adibi, “Improvement of Thermal Properties of Ultra-High Q Silicon Microdisk Resonators,” Conference on Lasers and Electro-Optics, CLEO/QELS 2008, San Jose, California, 4-9 May 2008.
 25. A. Eftekhar, M. Soltani, S. Yegnanarayanan, and A. Adibi, “Characterization of the Effect of Small Perturbations on the Optical Modes in High Q Microdisk Cavities,” Conference on Lasers and Electro-Optics, CLEO/QELS 2008, San Jose, California, 4-9 May 2008.
 26. E. Shah Hosseini, S. Yegnanarayanan, M. Soltani, and A. Adibi, “Optimization of SiN_x Planar Microdisk High Q Resonators for Chip-scale Visible Integrated Photonics,” Conference on Lasers and Electro-Optics, CLEO/QELS 2008, San Jose, California, 4-9 May 2008.
 27. M. Soltani, Q. Li, S. Yegnanarayanan, and A. Adibi, “Optimized Design of Flat-Band Finite-Size Coupled Resonator Optical Waveguides with Reduced In-Band Distortions,” Conference on Lasers and Electro-Optics, CLEO/QELS 2008, San Jose, California, 4-9 May 2008.
 28. E. Shah Hosseini, S. Yegnanarayanan, and A. Adibi, “Ultra-High Quality Factor Silicon Nitride Planar Microdisk Resonators for Integrated Photonics in the Visible Range,” Integrated Photonics and Nanophotonics Research and Applications, IPRNA 2008, (Optical Society of America), Boston, Massachusetts, 13 July 2008.
 29. Q. Li, S. Yegnanarayanan, A. Atabaki, and A. Adibi, “Calculation and Correction of Coupling-Induced Resonance Frequency Shifts in Traveling-Wave Dielectric Resonators,” Integrated Photonics and Nanophotonics Research and Applications, IPRNA 2008, Technical Digest (Optical Society of America), Boston, Massachusetts, 13 July 2008.
 30. S. Yegnanarayanan, W. Roman, M. Soltani, G. Cremona, Hang Lu, and A. Adibi, “On-chip Integration of Microfluidic Channels with Ultra-high Q Silicon Microdisk Resonators for Lab-on-a-Chip Sensing Applications,” IEEE Lasers and Electro-Optics Society, (LEOS), 20th Annual Meeting, Lake Buena Vista, Florida, 21-25 October 2007.
 31. M. Soltani, S. Yegnanarayanan, Q. Li, and A. Adibi, “Suppressing the Thermal Broadening/Instability of On-chip Ultra-high Q Silicon Microdisk Resonators,” IEEE Lasers and Electro-Optics Society, (LEOS), 20th Annual Meeting, Lake Buena Vista, Florida, 21-25 October 2007.
 32. M. Soltani, S. Yegnanarayanan, and A. Adibi, “Demonstration of Silicon Microdisk Resonators Compatible with Active Integration: Ultra-high Q and Efficient Waveguide-Resonator Coupling,” Conference on Lasers and Electro-Optics, CLEO/QELS 2007, Baltimore, Maryland, 6-11 May 2007.
 33. B. Momeni, E. Shah Hosseini, M. Askari, S. Mohammadi, M. Soltani, S. Yegnanarayanan, and A. Adibi, “Spectral Analysis in Integrated Optical Sensors Using Compact On-Chip Photonic Crystal

- Spectrometers,” Computational Optical Sensing and Imaging, Topical Meeting, Technical Digest (Optical Society of America), Vancouver, Canada, 18 June 2007.
34. S. Yegnanarayanan, Q. Li, M. Soltani, and A. Adibi, "Universal Parameters for the Design of Flat-band Finite-size Coupled Resonator Optical Waveguides," in *Slow and Fast Light*, Technical Digest (Optical Society of America), Salt Lake City, Utah, 8 July 2007.
 35. M. Soltani, S. Yegnanarayanan, Q. Li, and A. Adibi, "Silicon Pedestal Ultra-high Q Microdisk Resonators: A Novel Device Architecture to Suppress Thermal Instability and Enable Active Integration," Integrated Photonics and Nanophotonics Research and Applications, IPRNA 2007, Technical Digest (Optical Society of America), Salt Lake City, Utah, 8 July 2007.
 36. Q. Li, S. Yegnanarayanan, M. Soltani, and A. Adibi, "Systematic Design and Demonstration of Flat-Band Finite-Size Coupled Resonator Optical Waveguides," *Frontiers in Optics*, OSA Technical Digest (Optical Society of America), San Jose, California, September 16, 2007.
 37. M. Soltani, S. Yegnanarayanan, and A. Adibi, "Planar High-Q Microresonators for Chip-Scale Integrated Silicon Photonics," in Lasers & Electro-Optics Society, LEOS 2006 IEEE Lasers and Electro-Optics Society, (LEOS), 19th Annual Meeting, Montreal, Quebec, 29 October 2006.
 38. M. Soltani, S. Yegnanarayanan, and A. Adibi, "High-Q Silicon Microcavities for Chip Scale Integrated Optics," *Frontiers in Optics*, OSA Technical Digest (Optical Society of America), Rochester, New York, October 10, 2006.
 39. M. Soltani, S. Yegnanarayanan, and A. Adibi, "Design, Fabrication and Characterization of Photonic Crystal Directional Couplers," *Frontiers in Optics*, OSA Technical Digest (Optical Society of America), Rochester, New York, October 10, 2006.